A recipient-derived macrophages subset induces kidney allograft rejection through CXCL10 secretion and LILRB2 signaling

Alexis Varin[1‡], Jovanne Palvair[1‡], Lennie Messager[1‡], Jamal Bamoulid[1,2], Yacine Benchikh[1], Jasper Callemeyn[3], Mélanie Chaintreuil[4], Ludivine Dal Zuffo[1], Didier Ducloux[1,2], Imane Farhat[1,4], Mathieu Legendre[4], Laurent Martin[1,5], Florian Renosi[1], Xavier Roussel[1], Thibaut Vaulet[3], Maarten Naesens[3], Claire Tinel[1,4], Baptiste Lamarthée[1*]

Affiliations

[1]Université Marie et Louis Pasteur, EFS BFC, Inserm UMR Right, Besançon, France

[2]Department of Nephrology, Dialysis and Renal Transplantation, Besançon University Hospital, Besançon, France

[3]Department of Microbiology, Immunology and Transplantation, Nephrology and Kidney Transplantation Research Group, KU Leuven, Leuven, Belgium

[4]Department of Nephrology and Kidney Transplantation, Dijon University Hospital, Université Bourgogne-Europe, Dijon, France

[5]Department of Pathology, Dijon University Hospital, Université Bourgogne-Europe, Dijon, France

[‡]These authors equally contributed to this work.

*Corresponding author:

Baptiste Lamarthée, PhD

Phone: +33 3 81 615 615

8 rue du Dr Girod, 25000 Besançon, France

Email: baptiste.lamarthee@inserm.fr

Abstract

In solid organ transplantation, monocytes and macrophages play a cross-cutting role in the rejection process, irrespective of the transplanted tissue and the type of rejection. Here, we integrated multiple single-cell assays (>150,000 cells) with a broad spectrum of blood-derived and renal allograft-derived cells. We observed 6 cell trajectories enriched in the allograft during rejection, ranging from circulating CD14+ monocytes to differentiated macrophages in the kidney, with one trajectory culminating in a pro-inflammatory macrophage expressing CXCL9 and CXCL10. LILRB2, a gene encoding an HLA-binding receptor, was closely associated with this trajectory, and was found upregulated in a recirculating classical monocyte contingent in peripheral blood of patients with rejection but also in biopsies upon rejection. *In vitro*, allogeneic stimuli resulted in upregulation of LILRB2 in monocytes. Moreover, LILRB2 was able to bind non-self class I HLA in primary human macrophages resulting in overexpression of proinflammatory genes, suggesting the involvement of this receptor in monocyte/macrophage-associated rejection phenomena. Altogether, the present study provides further insight into the pro-inflammatory axes of recipient-derived monocytes/macrophages, and suggests LILRB2 as a therapeutic target.

Introduction

In the field of solid organ transplantation, graft rejection remains one of the major challenges to ensuring the survival and optimal function of the transplanted organ. While this phenomenon is influenced by various cell types and immune mechanisms[1], monocytes and macrophages play a crucial and cross-cutting role in the rejection process, regardless of the transplanted tissue or histological picture of rejection[2]. A recent study has notably consolidated a vast amount of transcriptomic data from multiple solid organ transplants, including kidney, heart, liver, and lungs, revealing a common feature in the rejection of these organs: myeloid cell-driven inflammation[3]. This study identified the myeloid-derived CXCL9 and CXCL10 chemokines as central players in this inflammatory process, highlighting a shared mechanism of rejection across different transplanted tissues[4]. The ability of CXCL9 and CXCL10 chemokines to be induced in pan-organ rejection, is reflected by the fact that they form excellent biomarkers of rejection[5–8], as illustrated by their routine measurement in the urine of kidney transplant patients to monitor immune quiescence[9]. Interestingly,

this research suggests that current phenotypes of rejection, against a background of T-cell targeted immunosuppression, does not longer appear to be primarily mediated by antibodies or T lymphocytes, but rather by monocytes and macrophages.

Additionally, three decades of animal model research demonstrate that monocytes are not merely passive players in the immune response but are capable of directly recognizing allogeneic tissues[10]. These studies have showed that monocytes, independently of the adaptive immune response, can initiate[11] and sustain alloimmune rejection[12]. This capacity of monocytes and macrophages to act as primary drivers of histological lesions, through mechanisms outside the classic T and B cell responses[13] reinforces their central role in the immune response to pan-organ transplants. These findings challenge the prevailing understanding of rejection by the adaptive immune system and emphasize the central role of myeloid cells in the inflammatory response leading to graft failure.

Monocytes and macrophages are particularly involved through their ability to infiltrate the allograft, contributing to the initiation and amplification of the immune response and the progressive degradation of the graft. However, despite their recognized importance, the precise mechanisms by which circulating monocytes, infiltrate the transplanted organ and differentiate into fully functional macrophages within the renal graft remain largely unknown.

Here, we aimed to conduct an in-depth analysis of myeloid cell populations in the context of kidney graft rejection. By leveraging single-cell sequencing technologies, we established a high-resolution cellular profile of over 150,000 cells derived from the blood of 13 patients (including 5 without rejection and 8 with rejection) and from kidney grafts of 33 patients (15 without rejection and 18 with rejection). We identified differentiation trajectories from circulating monocytes to tissue-resident macrophages and we identified key genes such as *FCN1*, *LILRA2*, *LILRB2, LILRA5, LST1* and *LY6E* involved in the differentiation of proinflammatory macrophages driving graft rejection. Finally, we explored *in vitro* and *in vivo* the significance of these molecules in allogeneic myeloid responses .

Results

Single-cell integration of kidney allograft and blood-derived cells

To characterize the infiltration of circulating monocytes and their differentiation into macrophages in kidney transplant patients, we integrated 46 single-cell RNA-Seq datasets, including

13 datasets corresponding to blood-derived cells (including N=5 without rejection and N=8 rejections) and 33 datasets corresponding to kidney allograft-derived cells (including N=13 without rejection and N=20 rejections, **Figure 1a**). The rejection phenotypes were diverse from a histological point of view and showed varying levels of inflammation, ranging from mild to severe. In addition, for N=3 patients, including two cases of rejection, we were able to integrate both blood cells and cells from the kidney allograft collected on the same day, contributing to the robustness of the results (**Figure 1b**). After passing quality controls (**Figure S1a**), we successfully integrated 150,876 transcriptomes without any major batch effects, whether between datasets, tissue of origin, or between the rejection group compared to the non-rejection group (**Figure S1b**). In an unsupervised manner, 23 different clusters were identified, corresponding to blood and kidney cells. The annotation using canonical and unsupervised markers (**Figure 1c, Supplemental Table 1**) of these clusters led to the identification of immune cells subtypes such as *S100A12+ LYZ+ CD14+* monocytes and *C1QA+ C1QB+ MS4A4A+* macrophages (**Figure 1d**). When comparing the proportion of immune cells between the rejection and non-rejection groups within the allograft, an increase in the proportion of immune cells was observed in cases of rejection, as expected. Notably, the proportion of macrophages within the allograft increased from 1.19% in non-rejection to 3.95% in cases of rejection (**Figure 1e**). A global, unsupervised comparison of the main cellular interactions between rejection and non-rejection on all integrated cells reveals that the no rejection group is mainly associated with CCL5 and LGALS9 (**Figure 1f**). In contrast, the rejection group is predominantly associated with CXCL10 and CXCL9 in line with recently reported pan-organ transcritomic data across organs, which confirms that CXCL9 and CXL10 chemokines are central in rejection process[3] and underscore the ubiquitous role of myeloid cells in solid-organ transplantation[4].

A pro-inflammatory macrophage subpopulation expressing *CXCL10* is specifically enriched during rejection

We then selected all the myeloid cells annotated previously as 'Monocyte' and 'Macrophage' (**Figure 1d**) for reintegration, in order to better understand the heterogeneity of myeloid cells, both in the blood and infiltrating the allograft after kidney transplantation. We thus obtained 11 different clusters in an unsupervised manner (**Figure 2a**). Among them, we identified in an unsupervised approach 6 monocyte populations and their specific markers (**Supplemental Table 2**), such as *S100A12+ CD14+ LYZ+* classical monocytes, a *MARCO+ APOBEC3A+* population of intermediate

monocytes, an *IFIT1*+ *HERC5*+ *MX1*+ population of IFN-activated monocytes, a *FCGR3A*+ *CDKN1C*+ non-classical monocyte population, a *PECAM1*+ *CX3CR1*+ *TCF7L2*+ patrolling monocyte population, and a monocyte population differentiating into dendritic cells, the mo-DCs expressing *AHNAK* and *HIST1H1E*. In addition, 3 populations of dendritic cells were detected: a *CLEC10A*+ *CD1C*+ *FCER1A*+ conventional type 2 DC (cDC2), a *CLEC9A*+ *XCR1*+ *GCSAM*+ cDC1 population and a *TNF*+ *CCL3L1*+ *CD83*+ population named hereafter "*CD83* mature DC". Finally, 2 subtypes of macrophages were distinguished from all other myeloid cells: a *SELENOP*+ *STAB1*+ *TREM2*+ population and a *CXCL10*+ *ANKRD22*+ population (**Figure 2b**). Concerning the proportion of the overall myeloid compartment detected within allografts, we observed a substantial increase with a doubling of the global myeloid population during rejection (**Figure 2c**) in line with previous reports[2,14]. More specifically, the infiltration ratio of myeloid cells differed according to their subtypes. While the proportion of cDC1, cDC2, CD83+ DC, mo-DC and patrolling monocyte was not enriched in allograft, the proportion of *CXCL10*+ macrophages, classical, intermediate and IFN-activated monocytes and *SELENOP*+ macrophages was statistically increased in rejection. In particular, a 5-fold increase in the proportion of *CXCL10*+ macrophages was observed, indicating a major enrichment of this population within the kidney allograft during rejection (**Figure 2d**). Among myeloid cells detected solely within the allograft, the proportion of *CXCL10*+ macrophages increased significantly in rejection (0.0% vs 6.4%, P=0.0009) compared with *SELENOP*+ macrophages (29.2% vs 25.4%, P=0.68) suggesting that not only infiltration but also differentiation of this population is directly associated with the allogeneic response against the graft (**Figure 2e**).

CXCL10+ and _SELENOP_+ macrophages harbor distinct transcriptomic programs

By comparing the transcriptomic profiles of the two macrophage populations (CXCL10+ and SELENOP+), we observed that *CXCL10*+ macrophages also overexpressed 112 signature genes, including proinflammatory genes such as *WARS*, *CXCL9*, *GBP1*, *GBP2* and *GBP5* which have previously been described as major biopsy-derived transcripts associated with rejection[15]. It is noteworthy that among these signature genes of *CXCL10*+ macrophages, a third is included in the Banff Human Organ Transplant (B-HOT) probe set panel[16] including pertinent genes related to rejection and innate and adaptive immune responses (N=36/112, **Supplemental Table 3**). Moreover, they specifically express genes encoding LILR receptors, some of which, such as LILRB1 and LILRB2, can bind HLA molecules[17]. In a reductive manner, macrophage subtypes have historically been

stratified according to pro-inflammatory M1[18] and pro-fibrotic M2[19] profiles obtained after *in vitro* differentiation from monocytes. We compared the transcriptomic profiles of *CXCL10*+ and *SELENOP*+ macrophages identified *in vivo* with M1 and M2 macrophages generated *in vitro*[20]. In *CXCL10*+ macrophages, 71.8% of their signature genes corresponded to genes upregulated in M1, revealing around 30% of "discordant" genes, including *S100A4* and *S100A6*, responsible for cell mobility. As for *SELENOP*+ macrophages, only 32.7% of their signature genes were shared with M2, suggesting that the historical stratification between M1 and M2 derived from *in vitro* experiments is too limited and cannot be directly matched to macrophage subtypes described *in vivo*[21] (**Figure S2a**). We then examined the origin of the two types of macrophages using the expression of X-linked genes or Y-linked genes as previously described in patients who had received a transplant from a sex other than their own[22]. Unambiguously, we observed that 100% of CXCL10+ macrophages originated from the recipient, suggesting that the presence of these cells entirely relies on infiltration by circulating monocytes. *SELENOP*+ macrophages, on the other hand, comprise around 18% donor-derived cells and 82% recipient-derived cells, so partly tissue-resident (**Figure S2b**). A comparison of the markers of these two subsets revealed that donor-derived *SELENOP*+ are *SELENOP*^{hi} and *TREM2*-, while recipient-derived *SELENOP*+ are *SELENOP*^{low} and *TREM2*+ (**Figure S2c**). In term of cellular interactions predicted at transcriptomic level between *CXCL10*+ and *SELENOP*+ macrophages and their microenvironnement in the allograft, we detected more than 35 significantly enriched incoming signaling and more than 40 outgoing signaling (**Figure S2d**). Among incoming signaling, we notably detected cell-contact CD47-SIRPA and LILRA1-B1-B2-class I HLA signaling which have been reported as responsible of allogeneic myeloid response in the animal[23,24] but also PECAM1-CD38, the interaction which is required for leukocyte transendothelial migration suggesting that the *CXCL10*+ macrophages derive from recipient-derived monocytes. In contrast, PECAM1-CD38 interaction was not detected in *SELENOP*+ macrophages suggesting that this population is less susceptible to derive from monocyte infiltrating the allograft through proinflammatory chemokine gradient (**Figure S2b**). In term of cytokine-receptors, *CXCL10*+ macrophages mainly receive TNF signaling through TNF-TNFRSF1 but also chemokines through CCL-CCR1. In return, *CXCL10*+ macrophages outgoing signaling is characterized by CXCL-receptors signaling and TNF signaling, suggesting both cis and trans-signaling through this pathway.

Myeloid cells differentiation is driven by six main trajectories in kidney transplant recipients

In order to better characterize the origin of the *CXCL10+* macrophages, we next built unsupervised pseudotime trajectories among myeloid cells. In the interests of transparency and reproducibility, our entire monocyte trajectory construction pipeline is publicly available. All of these trajectories originated from blood-derived classical monocytes and formed a branch at the level of intermediate monocytes, before being distributed in clusters of fully differentiated cells such as DCs and macrophages within the allograft, or as non-classical or patrolling monocytes which were detected in both blood and allograft (**Figure 3a**). These data suggest that classical monocytes can differentiate into intermediate and then non-classical monocytes as is also the case in the event of systemic inflammation[25]. Surprisingly, one of the trajectories formed a loop passing through CD83 mature DC and back to classical monocytes. Moreover, the six trajectories begin to separate at the branching point annotated "3" corresponding to intermediate monocytes. We therefore wanted to investigate which transcripts were specific to segment 3-4 of the branched section corresponding to *CXCL10+* macrophages. For this purpose, we compared the transcripts associated with segment 3-4 of each trajectory (**Figure 3b**) considering only the most specific transcripts (Rank score>q99). We intersected the transcripts of each comparison and defined 22 transcripts which were highly associated to segment 3-4 of *CXCL10+* macrophages (**Figure 3c**). Among these 22 transcripts, 5 of them, *FCN1*, *LY6E*, *LILRA2*, *LILRB2*, *LST1* and *LILRA5* shared a similar profile and high expression (**Figure 3d**). In order to confirm the increased expression of these 5 genes during rejection in external global transcriptomics datasets, we queried the PROMAD atlas[3] (**Figure S3a**). In 21 external datasets encompassing the 6 genes of interest and representing over 2,500 biopsies, *FCN1* and *LST1* expression was found to be systematically significantly increased in the graft during rejection except in two datasets. *LILRA2* was significantly increased in 18/21 datasets, and *LILRB2* in 15/21 datasets, confirming the importance of these transcripts during rejection. *LILRA5* and *LY6E*, on the other hand, were only significantly increased in 7/21 datasets indicating that they may be more specific to a subtype of immune response (**Figure S3b**). Plotting the expression of these genes along trajectories, we confirmed the specificity of these transcripts the *CXCL10+* macrophages trajectory. Surprisingly, we also observed that *LILRB2*, *LILRA5* together with *LILRA2* transcripts were upregulated at the end of the CD83 mature DC trajectory back to classical monocytes (**Figure 3e**). In mice, myeloid allorecognition is primed by CD47/SIRP-α axis[23] and leads to the overexpression of paired immunoglobulin receptors (PIRs) at myeloid cell surface[24]. The human orthologs of PIRs are leukocyte immunoglobulin-like receptors (LILRs). Here, our data suggest that the trajectory of *CXCL10+*

macrophages relies on three LILRs, *LILRB2, LILRA2* and *LILRA5,* but also that recirculating monocytes may retain the imprint of their passage through the allograft. We therefore expanded our analysis to the other LILRs and observed that *LILRA1*, *LILRB1* and *LILRB3* also follow the same expression profiles: they are strongly increased in *CXCL10*+ macrophages and they are upregulated at the end of the trajectory returning to classical macrophages (**Figure S4**).

We then investigated whether this activated state due to the allogeneic responses could be captured in the blood of kidney transplant recipients. For this purpose, we built an ancillary cohort to the ORLY-EST cohort of kidney transplant recipients[26]. For each patient, a blood sample was collected on the day of transplantation (d0) and one year later (d365) (**Figure 4a**). We therefore gathered N=64 patients with a pair of available PBMC samples (**Figure S5a**). Of these patients, 8 showed mild to very severe rejection during the first year of transplantation (**Figure S5b**). In order to perform a cytometric analysis limiting the potential batch effect, we followed a robust pipeline including batch correction and normalization (**Figure S5c**). We then applied a gating strategy using CD14 and CD16 markers to select CD14+CD16- classical monocytes, CD14+CD16+ intermediate monocytes and CD14-CD16+ non-classical monocytes (**Figure S5d**). By comparing the kinetics of LILRA1, LILRA2, LILRA5, LILRB1 LILRB2 and LILRB3 expression in these 3 populations between before transplantation and one year after, we observed that LILRA2 ($GeoMFI_{d0}$ = 509 vs $GeoMFI_{d365}$ = 626, P=0.046), LILRB1 ($GeoMFI_{d0}$ = 565 vs $GeoMFI_{d365}$ = 699, P=0.035) and LILRB2 ($GeoMFI_{d0}$ = 1369 vs $GeoMFI_{d365}$ = 1737, P=0.032) expression increases significantly in classical monocytes from patients with rejection compared with those without rejection. Moreover, this increase was not observed in intermediate or non-classical monocytes (**Figure 4b**). Altogether, these results suggest that upon rejection, classical monocytes could differentiate into CXCL10+ macrophages and infiltrate the allograft or recirculate with the imprint of allogeneic activation.

Allogeneic activation of classical monocytes leads to increased expression of LILRB2

Recent data from allogeneic recognition models in mice suggest that allogeneic monocytes are activated via the CD47-SIRP-α axis[23]. We hypothesized that this activation could drive the differentiation of recipient-derived monocytes into CXCL10+ macrophages. To recapitulate the impact of the allogeneic activation in circulating classical monocytes within the allograft, we thus activated them *in vitro* by the CD47-SIRP-α axis. For this purpose, classical monocytes were isolated from the

blood of healthy volunteers and an immunological synapse was artificially mimicked as is widely and historically done for T cells by activating their CD3 and CD28 receptors with antibodies coated onto the culture plastic[27]. Here, we used polyclonal antibodies targeting CD47, essential for myeloid allo-activation[10] and measured the impact of these activations at protein levels after 48h of culture (**Figure 5a**).

Forty-eight hours after activation, LILRA2 was not differentially expressed at cell surface. In contrast, LILRB2 and LILRA5 were significantly increased after stimulation of CD47 ($GeoMFI_{Ig}$ = 74975 vs $GeoMFI_{CD47}$ = 99030, P=0.0273 for LILRB2 and $GeoMFI_{Ig}$ = 1439 vs $GeoMFI_{CD47}$ = 2338, P=0.0137 for LILRA5) compared with control condition. The expression of CD16 ($GeoMFI_{Ig}$ = 6314 vs $GeoMFI_{CD47}$ = 12952, P=0. 0371) was also doubled after CD47 stimulation. Surprisingly, LILRB1 expression was significantly decreased ($GeoMFI_{Ig}$ = 26987 vs $GeoMFI_{CD47}$ = 20437, P=0.0059 , **Figure 5b-c**). Altogether these results suggest that the allogeneic recognition of SIRP-α via CD47 induces specifically certain LILRs such as LILRB2 and the differentiation from classical CD14+CD16- to intermediate CD14+CD16+ phenotype before macrophage differentiation.

Of note, *SIRPA* expression was primarily reported in myeloid cells but could also be detected in renal cells such as podocytes[28–30]. In addition, our cell-cell contact analysis suggested that CD47-SIRP-α signaling in *CXCL10*+ macrophages relies on *SIRPA* expression in both *SELENOP*+ macrophages and PT_injured cells (**Figure S2d**). We thus assessed the expression of *SIRPA* across all renal cell types and we confirmed that *SIRPA* is expressed in both podocytes and injured PT cells notably upon rejection (**Figure S6**). These results suggest that *CXCL10*+ macrophages could continue to be activated through CD47-SIRP-α in the tubulointerstitial compartment or in the damaged glomeruli within the allograft in addition to LILRs ligation.

Macrophages overexpressing LILRB2 bind HLA class I molecules, triggering their activation

We then wanted to explore the impact of LILRB2 overexpression in macrophages. To do this, we started with a human myeloid cell line, the THP-1 cell line[31], which, according to a previous report, lost LILRB2 expression on its surface compared with primary human monocytes[32]. We set up a transduction strategy with lentiviral vector encoding *LILRB2* and a reported gene, *TagBFP2* (**Figure S7a**). We then successfully isolated TagBFP2+ single cell clones by FACS and therefore generated 2 clones, D02 and G02, of THP-1 expressing high level of LILRB2 (**Figure S7b**). As LILRB2 is known to

bind to class HLA molecules present on the cell surface, unlike LILRA2 or LILRA5 [33,34], we next assessed whether LILRB2 overexpression could lead to a modulation of binding with HLA. Historically, THP-1 were described as HLA-A2+ and HLA-B5+[31]. We therefore verified that THP-1 express HLA-A2 and not HLA-B27 (**Figure S7c**) and we then tested the LILRB2-MHC interaction in THP-1 WT and clones D02 and G02. In THP-1 WT that do not express LILRB2, binding to self HLA (assessed by HLA-A2 pentamers) or non self HLA (HLA-B27 pentamers) is undetectable. In contrast, in LILRB2 overexpressing clones D02 and G02, we detected fixation of both self and non-self HLA (**Figure S7d**).

One of the limitations of the THP-1 model is inherent in the malignant nature of this cell line. We thus assessed the capacity of LILRB2-HLA interactions in *bona fide* primary human macrophages. In this aim, we adapted a similar lentiviral strategy in freshly isolated monocytes (**Figure 6a**). After 10 days of M0 differentiation, we measured the expression of both TagBFP2 and LILRB2 in the transduced macrophages and observed a significant increase of the percentage of LILRB2^{hi} cells (**Figure 6b-c**) compared with non-transduced control (Median $percent_{NT}$ = 0.00 vs Median $percent_{LILRB2}$ = 53.90 ; P=0.0022). We applied the same LILRB2-HLA interactions assay using HLA-A2 and HLA-B27 pentamers and were able to detect class I HLA binding on LILRB2^{hi} macrophages (**Figure 6d**). We confirmed that LILRB2 overexpression on the surface of primary macrophage binds both to HLA-A2 (Median $percent_{NT}$ = 1.09 vs Median $percent_{LILRB2}$ = 3.60 ; P=0.0078, **Figure 6e**) and HLA-B27 (Median $percent_{NT}$ = 16.61 vs Median $percent_{LILRB2}$ = 31.32 ; P=0.0273, **Figure 6f**) suggesting that LILRB2 expression on the macrophages surface can be part of the immunological synapse between recipient-derived pro-inflammatory *CXCL10*+ macrophages and donor cells.

A previous *in vitro* study has demonstrated that when LILRB2 is expressed on the surface of tolerogenic dendritic cells, it generates an antiproliferative signal to autologous T cells[35]. Here, we tested wether macrophages overexpressing LILRB2 would have an impact on the proliferation of autologous T cells (**Figure 6g**). Compared with activated T cells alone, the addition of M0 macrophages to the culture slightly reduced cell proliferation, potentially through competition for nutrients (**Figure 6h**). Interestingly, co-culture of LILRB2-overexpressing macrophages with T cells did not decrease T cell proliferation at a 1_{macro}:$1_{T\ cell}$ ratio. Moreover, at a 1_{macro}:$4_{T\ cell}$ ratio, T-cell proliferation increased significantly in the presence of macrophages overexpressing LILRB2 (P=0.0273, **Figure 6i**) suggesting that LILRB2 overexpression at macrophages surface can generate a signal that positively impacts autologous T cell proliferation.

Discussion

In the present study, we investigated circulating and allograft-infiltrating myeloid populations after kidney transplantation. To this end, we gathered a substantial amount of scRNA-Seq data from several study groups, several tissues (blood and biopsies) and several types of rejection in order to obtain a generalizable characterization of recipient monocyte/macrophage infiltration into the graft. Among the macrophage found within the allograft, we distinguished unsupervisely two main populations, *CXCL10*+ macrophages and *SELENOP*+ macrophages. In addition to rejection-associated *CXCL10*+ macrophages, we identified *SELENOP*+ macrophages as the main macrophagic subset populating the kidney allograft. *SELENOP*+ macrophages show a very distinct transptimomic profile as compare to *in vitro* differentiated M2 macrophages confirming that the M1-M2 classification is irrelevant in the context of allotransplantation and the description of macrophages *in vivo*. In line with our findings, Stewart and colleagues reported the existence of a subset of *bona fide* resident macrophages they annotated "MNP-d" and expressing high level of *SELENOP*, *C1QC* and *RNASE1* in the native kidney[36]. In addition, these *SELENOP*+ macrophages specifically express *CD81*, a marker for resident macrophages that is conserved in mammalian species and more specifically in mouse, rat, pig and human kidney tissue[37]. Intriguingly, among *SELENOP*+ macrophages, only recipient-derived macrophages resulting from differentiation and infiltration of circulating monocytes expressed the trigger receptor expressed on myeloid cells 2 (TREM2). *TREM2* was first described in macrophage infiltrating adipose tissue[38]. In kidney, a recent report showed an increase in TREM2+ infiltrating macrophages in both glomerular and tubulointerstitial compartments notably upon diabetes[39]. Here, we showed that donor-derived macrophages expressed high levels of *SELENOP* but not *TREM2* suggesting that TREM2 characterizes monocyte-derived macrophages that repopulate the kidney allograft after transplantation whereas *SELENOP*^{hi} macrophages could derive from self-renewal of donor macrophages.

In contrast, *CXCL10*+ macrophages are uniquely derived from recipient monocytes and are major contributors of allograft inflammation during rejection. In fact, this population dramatically increases during rejection and expresses massive levels of the proinflammatory chemokines *CXCL10* and *CXCL9.* Importantly, these chemokines have been confirmed in a recent large-scale transcriptomic study as essential mediators of rejection in all types of solid organ transplantation,

regardless of the transplanted organ or the subtypes of rejection[3]. Along with chemokine transcripts, *CXCL10+* macrophages also strongly express *GBP1, GBP4, GBP5* and *WARS,* suggesting that these transcripts detected in bulk transcriptomic obtained from allograft biopsy samples and forming genes signatures of rejection[15] originate primarily from this macrophage population. Importantly, WARS and GBP1 were confirmed as enriched at protein level in the allograft upon rejection[40,41]. *CXCL10+* macrophages also specifically express *ANKRD22* encoding Ankyrin repeat domain 22 (ANKRD22), a nuclear-encoded mitochondrial membrane protein that regulates mitochondrial Ca^{2+} and the Wnt pathway. *Ankrd22*$^{-/-}$ mice showed reduced inflammation by inhibiting macrophages tissue infiltration and TNF secretion after gastric mucosal injury[42]. It is noteworthy that upregulation of *ANKRD22* has previously been associated with macrophages activation in patients during kidney transplant rejection[43].

At ontogenic level, CXCL10+ macrophages originate from recipient-derived circulating classical monocytes. These differentiate into intermediate monocytes, then progress either to a non-classical monocyte phenotype, as reported in the context of systemic infection[25], or to macrophage differentiation. Importantly, we identified 6 core genes specifically associated with the CXCL10+ macrophages differentiation: *FCN1*, *LY6E*, *LST1*, *LILRA2*, *LILRB2* and *LILRA5.* Among these 6 genes, the expression of four of them, *FCN1, LST1, LILRA2* and *LILRB2*, is systematically increased in biopsies showing rejection, as shown by our external validations using the PROMAD atlas.

FCN1 encodes Ficolin-1, a protein localized in the secretory granules of monocytes cytoplasm. Mechanistically, Ficolin-1 forms active proteolytic complexes with MBL-associated serine proteases, activating complement via the lectin pathway[44]. Importantly, C4b deposition increases with the amount of Ficolin-1[45]. Whether *CXCL10+* macrophages can induce complement activation via Ficolin-1 sensing during kidney allograft rejection, independently of the humoral response remains to be investigated.

LY6E encodes a GPI-anchored cell surface protein called Lymphocyte antigen 6 complex locus E, which is involved in cell-cell adhesion and immunological synapse[46]. Further investigations must be pursued to determine the role of this protein in inflammatory macrophages infiltrating the graft.

LST1 is encoded within the Major Histocompatibility Complex class III region on the short arm of chromosome 6, specifically including genes encoding components of the complement system such as C2, C4 and cytokines such as TNF[47]. *LST1* is notably included in the B-HOT panel as one of the transcripts most implicated in solid organ rejection[16]. It is highly polymorphic and its rs2256965 single

nucleotide polymorphism is associated with a susceptibility for nephritis in systemic lupus erythromatosus patients[48].

LILRB2, *LILRA2* and *LILRA5* encode LILRs which have been shown to be essential in the allorecognition process of myeloid cells[17,24]. Like *LST1, LILRB2* is also included in the B-HOT panel [16]. Interestingly, cross-linking LILRA5 on the surface of monocyte induces the mobilization of calcium, a known signaling mediator that is released during cell activation. In addition, triggering of LILRA5 on monocytes induces the secretion of interleukin-1β (IL-1β), tumor necrosis factor-α (TNF-α), and IL-6. IL-1β, TNF-α, and IL-6 are normally released in the early stages of inflammatory responses, suggesting that LILRA5 might play a role in modulating monocyte function in inflammatory settings[49]. While the ligand of LILRA5 and LILRA2 is still unknown[34], LILRB2 has been reported as a putative binder for HLA class I[50], which was previously confirmed *in vitro* in transfected 293T cells and *ex vivo* in CD14- myelomonocytic cells[51]. Here we showed that after CD47/SIRP-α activation, classical monocytes overexpress LILRB2 on their surface together with CD16, suggesting that they initiate their differentiation into intermediate-monocytes. Moreover, this increase of LILRB2 in classical monocytes was also detected in the blood of patient with rejection one year after transplantation compared to patients with no rejection. Whether this increase in LILRB2 in circulating monocyte might reflect some myeloid immune memory towards nonself HLA in patients, as suggested in mice[24], remains to be validated in larger cohorts in which SIRP-α mismatches can be monitored. Interestingly, a population of pro-inflammatory macrophages strongly expressing LILRB2 has been reported to infiltrate the synovium of patients with rheumatoid arthritis[52]. LILRB2 was historically described as inhibitory because it includes ITIMs motifs at its intracellular part but it was recently reported that PirB/LILRB2 were expressed in hepatic macrophages and bound with their NASH-associated ligand ANGPTL8 to trigger the recruitment of macrophages to the liver, providing evidence that the LILRB2/PirB-ANGPTL8 axis could be a pathogenic driver of NASH pathogenesis and fibrogenesis. Notably, an PirB/LILRB2-ANGPTL8 interaction facilitates the differentiation of hepatic macrophages to a proinflammatory phenotype by enhancing the phosphorylation of P38, AKT, and P65 signals, which in turn causes an aggravation in hepatocyte lipid accumulation and an exacerbation from simple hepatic steatosis to steatohepatitis. This report also uncovers a function of PirB/LILRB2 receptors in monocytes migration which is in line with the present study[53] showing a specific increase in LILRB2 expression in recipient monocytes/macrophages infiltrating the allograft. Of note, ANGPTL8 is liver-specific and the LILRB2

ligand in kidney transplantation context remains to be characterized. Here, we showed that LILRB2 overxpression at macrophage's surface can bind class I HLA and does not induce any antiproliferative signal to autologous T cells, suggesting that the increase of LILRB2 at *CXCL10*+ macrophages cell surface does not limit recipient T cells response during rejection. Instead, our results suggest that LILRB2 expressed by monocytes and then *CXCL10*+ macrophages delivers an inflammatory signal to the myeloid cell in the allogeneic context. Our study does not allow us to conclude that it is the binding of LILRB2 to non-self HLA that induces this differentiation into *CXCL10*+ macrophages. For this, further investigations are required.

Our study has several limitations: we were unable to confirm the inflammatory monocyte/macrophage trajectories in another external dataset, but this work could be conducted in the coming years as the number of scRNASeq studies in human kidney transplantation increases every year. Spatial transcriptomics analyses would also allow us to better characterize the profile of CXCL10+ macrophages. It should be noted, that very recently, a spatial transcriptomics approach was carried out on FFPE-included renal graft biopsies, corroborating our findings. In this study, they confirm that monocytes and macrophages expressing *FCGR3A* are central to graft rejection, whatever the subtype of rejection. Using this new technique, they confirm that the *CXCL9*, *CXCL10*, *WARS*, *GBP1* and *GBP4* transcripts, which are CXCL10+ macrophages-specific transcripts as we described here, are universal transcripts associated with acute rejection. They also demonstrate upregulation of *CD47* and *SIRPA* in both TCMR and AMR suggesting that this CD47/SIRP-α axis is relevant in our study in order to investigate monocyte activation during allograft rejection[54].

In addition, we were unable to integrate scRNASeq data from patients with non-AMR rejection and thus cannot conclude that blood monocytes behave in exactly the same way as in AMR or stable patients with this type of rejection. Nevertheless, given that intragraft chemokine secretion measurable in urine is increased in both AMR and TCMR, this may indicate that monocyte trajectories are similar in both types of rejection. Furthermore, our *in vivo* flow cytometry study of LILRs expression in patient blood is monocentric and limited by its small size. Moreover, it includes only a single post-transplant time point and does not allow us to speculate on the modulation of monocyte LILRB2 in the longer term. Larger-scale confirmations at several post-transplant timings are needed to demonstrate increased LILRB2 expression in classical monocytes, which may reflect allogeneic activation. Finally, our *in vitro* analyses on the impact of LILRB2 in inflammatory macrophages remains limited by the use of differentiation by LPS and IFN-γ which, as we have shown, does not 100% reflect the profile of

CXCL10+ macrophages found within the graft. Of note, several teams have proposed and developed strategies to target monocytes and macrophages as a whole, with promising and encouraging results in the context of kidney transplantation [55–57].

The present study provides further insight into the pro-inflammatory axes of recipient-derived monocytes/macrophages, and suggests LILRB2 as a therapeutic target.

Methods

Single-cell RNA-sequencing data analysis

Main object generation:

The current study is a retrospective analysis of 46 publicly available single-cell RNASeq datasets from kidney transplanted patients, either peripheral blood mononuclear cells (PBMCs) or allograft-derived cells harvested from kidney biopsies. Raw data were downloaded either from the NCBI's Gene Expression Omnibus database (accession number: GSE145927[58], GSE171374[59] and GSE140989[60]), from BioStudies (accession number E-MTAB-11450[61] and E-MTAB-12051[62]) or from NCBI's BioProject (accession number: PRJNA974568[63]). Counts matrices were filtered using the following parameters: cells having <300 and >10000 genes detected and circulating cells presenting >10% mitochondrial transcripts were excluded whereas biopsy-derived cells presenting >25% mitochondrial transcripts were excluded. Filtered gene expression matrices were then merged into a single object, normalized and scaled. The top 2000 most variable genes were calculated prior to integration using rpca method from Seurat R package version 5.0.1[64], on the supercomputer facilities of the Mésocentre de Franche-Comté UMAP coordinates were calculated using the top 50 principal components (PC) and visualized with Seurat's DimPlot function. Unsupervised clustering was performed using Seurat's FindNeighbors and FindClusters functions with a resolution of 0.47, which led to the identification of 23 distinct clusters. Cell types were annotated by comparing the most differentially expressed genes (DEG) in each cluster, calculated using Seurat's FindAllmarkers function, with canonical markers from the litterature[58–63,65–70]; some highly specific DEG found in each cluster and previously unreported in the literature were also highlighted alongside canonical markers. Dot plots and cell proportion barplots were generated using respectively the DotPlot_Heatmap and Barplot_Cell_Proportion functions from the R package RightOmicsTools version 2.2.0[71], with normalized counts as input data.

Myeloid cells reintegration:

Cells identified as monocytes, macrophages and cDC were subsetted from the main object and reintegrated in order to determine their cell subtypes composition. Briefly, the top 2000 most variable genes were recalculated, prior to a new integration with rpca method. UMAP coordinates and unsupervised clustering were calculated using Seurat's respective functions on the top 50 PC and a resolution of 0.85, which led to the identification of 11 distinct clusters. Annotation was performed on Seurat's FindAllMarkers top DEG in each cluster and compared to canonical markers from the literature[58–63,72,73]. Seurat's FindMarkers function was used to find DEG between *SELENOP*+ macrophages and *CXCL10*+ macrophages, and a volcano plot was built from the -log10 transformed FDR adjusted p-values and the log2 fold change values for each gene using ggplot2; the significance cutoff was set to a -log10 transformed FDR adjusted p-value of 15 and a log2 fold chance below -1.5 or above 1.5.

Determination of myeloid cell origin

Two genes signatures were built from a set of 3 genes specific to either chromosome X (*XIST*, *JPX* and *FTX*, thereafter designated as "female signature") or chromosome Y (*DDX3Y*, *KDM5D* and *USP9Y*, thereafter designated as "male signature") and a module score was calculated on biopsy-derived scRNASeq samples for each signature using the R package UCell version 2.6.2[74]. Datasets showing a sex mismatch between the donor and the recipient with a clear opposing signatures expression observed using the blend parameter of Seurat's FeaturePlot function were selected for further analysis: TAC1, TAC2, TAC3, TAC4, BELA2, BELA3, GSM4339776, GSM4339779, EXT241, NEPH012, NEPH016, NEPH017 and NEPH019. Cell identities were obtained from the blended FeaturePlot's ggplot2 object using ggplot2's ggplot_build function and then matching the data (x and y coordinate values of the scatterplot) of colored cells positive for either signature with UMAP's cell embeddings.

Cell-cell communication analysis

The R package CellChat version 2.1.2[75] was used to investigate ligands-receptors interactions between cell types and unravel communication networks. Annotations from reintegrated myeloid cells were transferred onto the same cells in the main object (matching cell barcode IDs from both objects) using Seurat's SetIdent function. The CellChat database was appended to add interactions or modify existing interactions based on published data[76–78]. A CellChat object was created from the normalized counts matrix and annotations of the main Seurat object and overexpressed genes, interactions, and

communication probabilities were computed using CellChat's respective functions identifyOverExpressedGenes, identifyOverExpressedInteractions, computeCommunProb (with TriMean type), filterCommunication (minimum 10 cells), computeCommunProbPathway, aggregateNet and netAnalysis_computeCentrality. Incoming and outgoing interaction strength were visualized using CellChat's netAnalysis_signalingRole_scatter function. Networks of ligands-receptors pairs were generated using the cc_network function from the R package CCPlotR version 0.99.3[79].

Trajectory inference analysis

The R package slingshot version 2.10.0[80] was used to explore trajectories/lineages in myeloid cells[51]. The cell embeddings matrix corresponding to UMAP coordinates of reintegrated myeloid cells was used as input for pseudotime inference using slingshot's slingshot function, with classical monocytes as starting cluster. Custom functions were developed for trajectories visualization on UMAP coordinates using ggplot2 version 3.5.1 and patchwork version 1.2.0 R packages and slingshot's slingPseudotime and slingCurves functions to extract inference results data for plotting.

Trajectory-based differential expression analysis

The R package tradeSeq version 1.16.0[81] was used to find key genes significantly associated with each trajectory identified by slingshot. The raw counts matrix of reintegrated myeloid cells was filtered using the RightOmicsTools's tradeSeqPreprocess function, keeping genes only expressed in more than 10 cells and removing mitochondrial, ribosomal and non-coding genes, in order to reduce computational burden without losing much information, poorly represented genes being unlikely to contribute; 13,981 genes passed the selection. The filtered raw counts matrix as well as the slingshot output converted into a SlingshotDataSet object were first used as input to tradeSeq's evaluateK function, which determines the number of knots to fit on each trajectory for differential expression analysis. Upon selecting 5 knots based on evaluteK results, the same input objects were then used to fit a negative binomial generalized additive model (NB-GAM) for each gene on each trajectory using tradeSeq's fitGAM function on the supercomputer facilities of the Mésocentre de Franche-Comté. Computation time was greatly reduced using parallel computing from BiocParallel version 1.36.0 and batchtools version 0.9.17 R packages; a custom Slurm template was created and used as input to BiocParallel's BatchtoolsParam function to take advantage of the scheduler capacity to automatically

divide calculations into individual jobs, submit them in parallel to cluster nodes, and retrieve results from within the R environment. Within lineage DEG comparison was performed using RightOmicsTools's tradeSeqTests function, which is a wrapper around tradeSeq's earlyDETest adding FDR adjusted p-value and tidying the data, between knot 3 and 4 with fitGAM results as input. A rank score was built from the results of each of these statistical tests, corresponding to $(\boldsymbol{Wald\ statistic\ rank})^2 + (\boldsymbol{mean\ or\ median\ log2\ fold\ change\ rank})^2$ (as computed by the R base rank function, with ties randomly broken) and the squared mean or median log2 fold change rank for each gene on each lineage or within lineage comparison, and plotted alongside the log10 transformed Wald statistic values and log10 transformed mean or median log2 fold change values for each gene using a custom ggplot2 code. Genes corresponding to the 90th percentile and up in terms of rank score (as computed by the R package stats's quantile function, with 0.9 probability) from each lineage or within lineage comparison were selected and visualized on Venn diagrams, produced using the R package venn version 1.12. Knots on trajectories were visualized on UMAP coordinates using tradeSeq's plotGeneCount function and a custom ggplot2 code. Scatterplots, smoothed gene expression curves and pseudotime heatmaps were generated respectively by the RightOmicsTools's curveSmoothers and heatmapSmoothers functions.

Interrogation of the PROMAD atlas

The online atlas tool was used to retrieve relative expression data for *FCN1*, *LILRA2*, *LILRA5*, *LILRB2, LST1* and *LY6E* in kidney biopsies from the control or acute rejection groups (https://shiny.maths.usyd.edu.au/PROMAD/). Only the 21 rejection datasets including the 6 genes of interest were considered here. After selecting the datasets on the tool, the object in RDS format was downloaded, and the expression data corresponding only to the 6 genes of interest were extracted in R. These data were then statistically compared between groups using Prism software for each of the datasets indicated using two-tailed Unpaired t test.

M1 and M2 macrophages bulk RNA-sequencing data analysis

Raw data were downloaded from the NCBI's Gene Expression Omnibus database (accession number: GSE146028[20]) and loaded into BIOMEX software version 1.0.5[82]. Metadata corresponding to macrophages M1 and M2 subtypes were added, counts were normalized. A volcano plot of M1 vs M2 comparison was generated, DEG results used to build the plot (log2 fold change, p-value and FDR adjusted p-value) were exported into R and the volcano plot was reconstructed from these values

using ggplot2; the significance cutoff was set to a -log10 transformed FDR adjusted p-value of 2 and a log2 fold chance below -1.5 or above 1.5. Genes found to be significant on the volcano plot between *SELENOP*+ and *CXCL10*+ macrophages were represented and four quadrans were drawn depending on significance cutoff, with a fifth area representing no significance.

Isolation of PBMC by density gradient

Peripheral blood from Buffy coats (Etablissement Français du Sang-BFC, France) was filtered through a 70µm strainer. Two volumes of blood were poured onto one volume of Lymphocyte separation medium (Eurobio Scientific, Les Ulis, France). Cells were then centrifuged for 30 min at 800g at room temperature. PBMC were washed with Phosphate-Buffered Saline (PBS, Thermofisher, Courtaboeuf, France) by centrifugation at 450g at 4°C for 5min. The cell pellet was resuspended in PBS, then centrifuged at 2100g for 2min at 4°C to remove the platelets.

Flow cytometry analysis

Samples to be analyzed by flow cytometry were centrifuged at 700g 5min at room temperature. One million cells from each condition were labeled with fluorochrome-coupled antibody for 15min at 4°C. Prior to cytometric analysis, labeled cells were washed with 2mL PBS and centrifuged at 700g 5min at room temperature before being resuspended in 200 µL PBS for analysis on a DxFlex cytometer (Beckman Coulter, Paris, France) or an Attune cytometer (Thermofisher). The following antibodies were used: anti-LILRB2 PE-Vio 770 (REA184, Miltenyi Biotec), anti-CD16 BV605 (3G8, Biolegend). When indicated, incubation with Fixable Viability Stain 700 (BD Biosciences, Paris, France) was performed prior to incubation with the coupled antibodies according to the supplier's recommendations.

Monocyte sorting

Monocytes were magnetically sorted from PBMC either by the CD14 Microbeads kit for transduction experiments or by the PanMonocyte kit (Miltenyi Biotec, Paris, France) for *in vitro* activation experiments following the supplier's recommendations. A minimum purity of over 85% was required to start the experiments.

Monocyte activation

Anti-CD47 (PA5-80435, Thermofisher) and a non-specific control antibody (10500C, Thermofisher) were coated in a 12-well plate (3413, Corning) for 4h at 37°C at a concentration of 3µg/mL in PBS. The wells were then emptied and $0.5.10^6$ purified monocytes suspended in 1mL of warm RPMI supplemented with 10% FBS and 1% Pen/Strep medium were deposited in each well before spinoculation for 1min at 100g, followed by incubation at 37°C with 5% CO2.

Lentiviral transduction

To induce expression of the LILRB2 in THP-1, we used lentiviral strategy (VectorBuilder, Neu-Isenburg, Germany) with a lentivirus encoding *LILRB2* and a reporter gene encoding *TagGFP2*. THP-1 were transduced at a multiplicity of infection (MOI) of 2.5 in the presence of 8 mg/L Polybrene (PL001, VectorBuilder). Briefly, $0.5.10^6$ cells per well were seeded in P24 well plate in the presence of virus particles and Polybrene. Control wells contained only $0.5.10^6$ cells/well and culture medium. The transduction was performed by spinoculation, i.e. centrifugation at 32°C, 1000 g for 90 minutes before culture for 2 days. To induce expression of the LILRB2 in human primary macrophages, monocytes freshly isolated from healthy volunteers were subjected to M0 differentiation by M-CSF (130-096-492, Miltenyi Biotec) at 25ng/mL in X-Vivo medium (BEBP02-054Q, Lonza, Colmar, France) supplemented with 10% of FBS (10271-106, Gibco) for 2 days before transduction with virus-like particles packaging Vpx to overcome virus restriction[83]. The production of Vpx particles was performed as previously described[84]. At day 4 of culture, the cells were transduced with the lentivirus encoding *LILRB2* and *TagBFP2* at MOI 1. At day 10 of culture, the fully differentiated macrophages were collected for cytometry analysis and LILRB2-HLA interactions assay.

FACS isolation of THP-1 clones

Cell sorting of transduced THP-1s was performed using a BDFACS ARIA III sorter (BD Biosciences, Paris, France) at the ImaFlow Platform (Dijon, France). THP-1 cells were labelled with an anti-LILRB2 PE Vio 770. The clones expressing different levels of the reporter gene TagBFP2 were selected and sorted in a 96-well plate pre-filled with culture medium to obtain one single clone per well. Identification of each clone according to the expression levels of LILRB2 was performed on FlowJo software using the Index Sort plugin (BD Biosciences).

LILRB2-HLA interaction assay

In order to assess LILRB2-HLA interaction, cells of interest were incubated with HLA-B27-APC pentamer (F294-4B-E, ProImmune, Oxford, UK) or HLA-A2-A2-PE pentamer (F10-2B-E, ProImmune) according to the supplier's recommendations.

ORLY-EST ancillary cohort

ORLY-Est (Orientation of the Lymphocyte Response to the Occurrence of Atherosclerotic Complications After Kidney Transplantation, NCT02843867) is a prospective cohort study of kidney transplant patients included in seven French transplant centers (Besançon, Clermont-Ferrand, Dijon, Le Kremlin-Bicêtre, Nancy, Reims and Strasbourg), whose main objective was to understand the interactions between immune status and post-transplant outcomes. For each patient, blood samples were collected on the day of transplantation (d0) and one year later (d365). Peripheral blood mononuclear cells (PBMC) were separated by density gradient centrifugation (Pancoll, Pan-Biotech GmBH Aidenbach, Germany) and stored in liquid nitrogen at the Centre de Ressources Biologiques Ferdinand Cabanne (Dijon, France). Samples were collected with the regulatory approval of the French Ministry of Health (agreement number DC-2008-713 dated June 11, 2009), and the study was approved by the ethics committee of the Université de Franche-Comté in 2008. All patients included in the ORLY-Est study were of legal age at the time of transplantation, and gave written informed consent. For this ancillary present study, PBMC were stained for flow cytometry analysis as previously described in an 8-batch sequence including a common healthy PBMC for batch normalization. To ensure analysis quality, cytometry files were normalized between batches using the CytoNorm[85] plugin, and abnormal events intrinsic to cytometry were removed using the FlowClean[86] plugin.

Inflammation level analysis

A diagnostic label was awarded to each biopsy based on the presence and severity of these histological lesions and on the DSA status. In this aim, all biopsies were categorized into one of six recently described clinicopathological categories[87], based on the presence of acute histological lesions and recipient DSA status (available at https://rejectionclass.eu.pythonanywhere.com/). This data-driven classification allows for visualization of the biopsies on a two-dimensional polar plot in which the theta angle associates with the spatial localization of the inflammation, i.e., microvascular inflammation versus tubulointerstitial inflammation. The radius indicates the global severity of the inflammatory infiltrate given by the sum of re-weighted acute lesions scores, scaled to the unit interval (from 0 to 1) and is hereafter designated as "Activity index"[87,88].

Autologous T Cell Proliferation Assays

On the day of monocyte sorting, the remaining PBMC from the same donors were cultured in complete RPMI supplemented with IL-2. To achieve coculture with syngeneic macrophages, PBMCs were stained with Cell Trace Red according to the manufacturer's procedure (Cell Trace, Thermofisher). Labeled cells were cultured with human CD3/CD28 T activator beads (Dynabeads, Thermofisher) in a 96-well UBottom plate in 100µL of complete RPMI at $1{,}10^6$ cells/mL with or without 100µL of macrophages. For dose-dependent experiments, the number of labeled PBMC was fixed, while the number of macrophages varied from a ratio of 1:1 to 1:4 (macrophages:PBMC). T-cell division was detected after 5 days by flow cytometry and analyzed using the Proliferation module of FlowJo software.

Statistical analysis

We report descriptive statistics using mean and standard deviation (or median and interquartile range for skewed distributions) for continuous variables or numbers, and percentages for discrete variables, for the full cohort and for the rejection subgroups. We used the most recent (as of September 2024) versions of all software programs, including R Studio (version 2023.12.1+402) and GraphPad Prism (version 10; GraphPad Software, San Diego, CA, United States) for statistical analysis and data presentation.

Data availability statement

All omic data are already publicly available.

All data produced in the present study are available upon reasonable request to the authors

Code availability

The complete codebase developed for the unsupervised differentiation trajectory analysis of myeloid cells is publicly available as a Jupyter Notebook at https://github.com/InsermRightLab/LILRB2-Varin-et-al/. It provides a detailed, step-by-step walkthrough of the computational workflow used to generate each figure, encompassing pseudotime inference using slingshot and identification of differentially expressed genes via tradeSeq. The primary functions, especially those integral to the computational

workflow, have been consolidated into RightOmicsTools, an R package available at https://alexis-varin.github.io/RightOmicsTools/. Additional supporting code, including utility functions, is provided within the notebook repository to ensure transparency and reproductibility. Code for Seurat is available at https://satijalab.org/seurat/. Code for CellChat is available at https://github.com/jinworks/CellChat/. Code for slingshot is available at https://github.com/kstreet13/slingshot/. Code for tradeSeq is available at https://github.com/statOmics/tradeSeq/.

References

1. Callemeyn, J. *et al.* Allorecognition and the spectrum of kidney transplant rejection. *Kidney Int* (2021) doi:10.1016/j.kint.2021.11.029.
2. Calvani, J. *et al.* In situ multiplex immunofluorescence analysis of the inflammatory burden in kidney allograft rejection: A new tool to characterize the alloimmune response. *American Journal of Transplantation* **20**, 942–953 (2020).
3. Robertson, H. *et al.* Decoding the hallmarks of allograft dysfunction with a comprehensive pan-organ transcriptomic atlas. *Nat Med* (2024) doi:10.1038/s41591-024-03030-6.
4. Vaulet, T. & Naesens, M. Stronger together: the power of cross-organ data sets for improved allograft study outcomes. *Kidney Int* **106**, 783–786 (2024).
5. Park, S. *et al.* European Society of Organ Transplantation Consensus Statement on Testing for Non-Invasive Diagnosis of Kidney Allograft Rejection. *Transplant International* **36**, (2024).
6. Van Loon, E. *et al.* Automated Urinary Chemokine Assays for Noninvasive Detection of Kidney Transplant Rejection: A Prospective Cohort Study. *Am J Kidney Dis* **83**, 467–476 (2024).
7. Tinel, C. *et al.* Development and validation of an optimized integrative model using urinary chemokines for noninvasive diagnosis of acute allograft rejection. *American Journal of Transplantation* **20**, 3462–3476 (2020).
8. Rabant, M. *et al.* Urinary C-X-C motif chemokine 10 independently improves the noninvasive diagnosis of antibody-mediated kidney allograft rejection. *Journal of the American Society of Nephrology* **26**, 2840–2851 (2015).
9. Tinel, C. *et al.* Transforming kidney transplant monitoring with urine CXCL9 and CXCL10: practical clinical implementation. *Sci Rep* **14**, 20357 (2024).
10. Abou-Daya, K. I. & Oberbarnscheidt, M. H. Innate allorecognition in transplantation. *J Heart Lung Transplant* **40**, 557–561 (2021).
11. Oberbarnscheidt, M. H. *et al.* Non-self recognition by monocytes initiates allograft rejection. *Journal of Clinical Investigation* **124**, 3579–3589 (2014).
12. Fox, A., Mountford, J., Braakhuis, A. & Harrison, L. C. Innate and Adaptive Immune Responses to Nonvascular Xenografts: Evidence That Macrophages Are Direct Effectors of Xenograft Rejection. *The Journal of Immunology* **166**, 2133–2140 (2001).
13. Liu, W., Xiao, X., Demirci, G., Madsen, J. & Li, X. C. Innate NK Cells and Macrophages Recognize and Reject Allogeneic Nonself In Vivo via Different Mechanisms. *The Journal of Immunology* **188**, 2703–2711 (2012).
14. Bräsen, J. H. *et al.* Macrophage density in early surveillance biopsies predicts future renal transplant function. *Kidney Int* **92**, 479–489 (2017).
15. Halloran, P. F. *et al.* Review: The transcripts associated with organ allograft rejection. *American Journal of Transplantation* vol. 18 785–795 Preprint at https://doi.org/10.1111/ajt.14600 (2018).

16. Mengel, M. *et al.* Banff 2019 Meeting Report: Molecular diagnostics in solid organ transplantation–Consensus for the Banff Human Organ Transplant (B-HOT) gene panel and open source multicenter validation. *American Journal of Transplantation* **20**, 2305–2317 (2020).
17. Palvair, J. *et al.* The Potential Role of the Leucocyte Immunoglobulin-Like Receptors in Kidney Transplant Rejection: A Mini Review. *Transplant International* **37**, (2024).
18. Nathan, C. F., Murray, H. W., Wiebe, M. E. & Rubin, B. Y. Identification of interferon-gamma as the lymphokine that activates human macrophage oxidative metabolism and antimicrobial activity. *J Exp Med* **158**, 670–689 (1983).
19. Stein, M., Keshav, S., Harris, N. & Gordon, S. Interleukin 4 potently enhances murine macrophage mannose receptor activity: a marker of alternative immunologic macrophage activation. *J Exp Med* **176**, 287–292 (1992).
20. Gurvich, O. L. *et al.* Transcriptomics uncovers substantial variability associated with alterations in manufacturing processes of macrophage cell therapy products. *Sci Rep* **10**, 14049 (2020).
21. Pizzurro, G. A. & Miller-Jensen, K. Reframing macrophage diversity with network motifs. *Trends Immunol* **44**, 965–970 (2023).
22. Lamarthée, B. *et al.* Transcriptional and spatial profiling of the kidney allograft unravels a central role for FcyRIII+ innate immune cells in rejection. *Nat Commun* **14**, 4359 (2023).
23. Dai, H. *et al.* Donor SIRPα polymorphism modulates the innate immune response to allogeneic grafts. *Sci Immunol* **2**, eaam6202 (2017).
24. Dai, H. *et al.* PIRs mediate innate myeloid cell memory to nonself MHC molecules. *Science (1979)* **368**, 1122–1127 (2020).
25. Patel, A. A. *et al.* The fate and lifespan of human monocyte subsets in steady state and systemic inflammation. *Journal of Experimental Medicine* **214**, 1913–1923 (2017).
26. Bamoulid, J. *et al.* Pretransplant thymic function predicts acute rejection in antithymocyte globulin–treated renal transplant recipients. *Kidney Int* **89**, 1136–1143 (2016).
27. Riddell, S. R. & Greenberg, P. D. The use of anti-CD3 and anti-CD28 monoclonal antibodies to clone and expand human antigen-specific T cells. *J Immunol Methods* **128**, 189–201 (1990).
28. Kajiho, Y. *et al.* SIRP **α** interacts with nephrin at the podocyte slit diaphragm. *FEBS J* **279**, 3010–3021 (2012).
29. Takahashi, S. *et al.* SIRPα signaling regulates podocyte structure and function. *American Journal of Physiology-Renal Physiology* **305**, F861–F870 (2013).
30. Kurihara, H., Harita, Y., Ichimura, K., Hattori, S. & Sakai, T. SIRP-α-CD47 system functions as an intercellular signal in the renal glomerulus. *American Journal of Physiology-Renal Physiology* **299**, F517–F527 (2010).
31. Tsuchiya, S. *et al.* Establishment and characterization of a human acute monocytic leukemia cell line (THP□1). *Int J Cancer* **26**, 171–176 (1980).
32. Lu, H. K. *et al.* Leukocyte Ig-like receptor B4 (LILRB4) is a potent inhibitor of FcgammaRI-mediated monocyte activation via dephosphorylation of multiple kinases. *J Biol Chem* **284**, 34839–48 (2009).
33. Redondo-García, S. *et al.* Human leukocyte immunoglobulin-like receptors in health and disease. *Front Immunol* **14**, (2023).
34. van der Touw, W., Chen, H.-M., Pan, P.-Y. & Chen, S.-H. LILRB receptor-mediated regulation of myeloid cell maturation and function. *Cancer Immunology, Immunotherapy* **66**, 1079–1087 (2017).
35. Beinhauer, B. G. *et al.* Interleukin 10 regulates cell surface and soluble LIR□2 (CD85d) expression on dendritic cells resulting in T cell hyporesponsiveness *in vitro*. *Eur J Immunol* **34**, 74–80 (2004).

36. Stewart, B. J. *et al.* Spatiotemporal immune zonation of the human kidney. *Science (1979)* **365**, 1461–1466 (2019).
37. Zimmerman, K. A. *et al.* Single-Cell RNA Sequencing Identifies Candidate Renal Resident Macrophage Gene Expression Signatures across Species. *Journal of the American Society of Nephrology* **30**, 767–781 (2019).
38. Jaitin, D. A. *et al.* Lipid-Associated Macrophages Control Metabolic Homeostasis in a Trem2-Dependent Manner. *Cell* **178**, 686-698.e14 (2019).
39. Fu, J. *et al.* The single-cell landscape of kidney immune cells reveals transcriptional heterogeneity in early diabetic kidney disease. *Kidney Int* **102**, 1291–1304 (2022).
40. Chauveau, B. *et al.* WARS1, TYMP and GBP1 display a distinctive microcirculation pattern by immunohistochemistry during antibody-mediated rejection in kidney transplantation. *Sci Rep* **12**, (2022).
41. Chauveau, B. *et al.* The Proteome of Antibody-Mediated Rejection: From Glomerulitis to Transplant Glomerulopathy. *Biomedicines* **10**, 569 (2022).
42. Liu, J. *et al.* ANKRD22 Drives Rapid Proliferation of Lgr5+ Cells and Acts as a Promising Therapeutic Target in Gastric Mucosal Injury. *Cell Mol Gastroenterol Hepatol* **12**, 1433–1455 (2021).
43. Venner, J. M. *et al.* Molecular Landscape of T Cell–Mediated Rejection in Human Kidney Transplants: Prominence of CTLA4 and PD Ligands. *American Journal of Transplantation* **14**, 2565–2576 (2014).
44. Garred, P., Honoré, C., Ma, Y. J., Munthe-Fog, L. & Hummelshøj, T. MBL2, FCN1, FCN2 and FCN3—The genes behind the initiation of the lectin pathway of complement. *Mol Immunol* **46**, 2737–2744 (2009).
45. Liu, Y. *et al.* Human M-Ficolin Is a Secretory Protein That Activates the Lectin Complement Pathway. *The Journal of Immunology* **175**, 3150–3156 (2005).
46. Classon, B. J. & Boyd, R. L. Thymic□Shared Antigen□1 (TSA□1) A Lymphostromal Cell Membrane Ly□6 Superfamily Molecule with a Putative Role in Cellular Adhesion. *J Immunol Res* **6**, 149–156 (1998).
47. Rollinger-Holzinger, I. *et al. LST1*□: A Gene with Extensive Alternative Splicing and Immunomodulatory Function. *The Journal of Immunology* **164**, 3169–3176 (2000).
48. Mewar, D. *et al.* Haplotype-specific gene expression profiles in a telomeric major histocompatibility complex gene cluster and susceptibility to autoimmune diseases. *Genes Immun* **7**, 625–631 (2006).
49. Borges, L., Kubin, M. & Kuhlman, T. LIR9, an immunoglobulin-superfamily–activating receptor, is expressed as a transmembrane and as a secreted molecule. *Blood* **101**, 1484–1486 (2003).
50. Shiroishi, M. *et al.* Human inhibitory receptors Ig-like transcript 2 (ILT2) and ILT4 compete with CD8 for MHC class I binding and bind preferentially to HLA-G. *Proceedings of the National Academy of Sciences* **100**, 8856–8861 (2003).
51. Allen, R. L., Raine, T., Haude, A., Trowsdale, J. & Wilson, M. J. Cutting Edge: Leukocyte Receptor Complex-Encoded Immunomodulatory Receptors Show Differing Specificity for Alternative HLA-B27 Structures. *The Journal of Immunology* **167**, 5543–5547 (2001).
52. Tedla, N. *et al.* The Co-Expression of Activating and Inhibitory Leukocyte Immunoglobulin-Like Receptors in Rheumatoid Synovium. *Am J Pathol* **160**, 425–431 (2002).
53. Li, D.-P. *et al.* LILRB2/PirB mediates macrophage recruitment in fibrogenesis of nonalcoholic steatohepatitis. *Nat Commun* **14**, 4436 (2023).
54. Wongworawat, Y. C. *et al.* Spatial Transcriptomics Using Archived Formalin-Fixed Paraffin-Embedded Core Needle Biopsy Tissues Revealed Unique Transcriptomic Signatures in Kidney Transplant Rejections. *bioRxiv* 2025.04.08.647600 (2025) doi:10.1101/2025.04.08.647600.

55. Kitchens, W. H. *et al.* Macrophage depletion suppresses cardiac allograft vasculopathy in mice. *Am J Transplant* **7**, 2675–2682 (2007).
56. Jose, M. D., Ikezumi, Y., van Rooijen, N., Atkins, R. C. & Chadban, S. J. Macrophages act as effectors of tissue damage in acute renal allograft rejection. *Transplantation* **76**, 1015–1022 (2003).
57. Lai, C. *et al.* Targeting inflammatory monocytes by immune-modifying nanoparticles prevents acute kidney allograft rejection. *Kidney Int* **102**, 1090–1102 (2022).
58. Malone, A. F. *et al.* Harnessing Expressed Single Nucleotide Variation and Single Cell RNA Sequencing to Define Immune Cell Chimerism in the Rejecting Kidney Transplant. *Journal of the American Society of Nephrology* **31**, 1977–1986 (2020).
59. Cormican, S. *et al.* Chronic Kidney Disease Is Characterized by Expansion of a Distinct Proinflammatory Intermediate Monocyte Subtype and by Increased Monocyte Adhesion to Endothelial Cells. *Journal of the American Society of Nephrology* **34**, 793–808 (2023).
60. Menon, R. *et al.* Single cell transcriptomics identifies focal segmental glomerulosclerosis remission endothelial biomarker. *JCI Insight* **5**, (2020).
61. Van Loon, E. *et al.* Biological pathways and comparison with biopsy signals and cellular origin of peripheral blood transcriptomic profiles during kidney allograft pathology. *Kidney Int* **102**, 183–195 (2022).
62. Lamarthée, B. *et al.* Transcriptional and spatial profiling of the kidney allograft unravels a central role for FcyRIII+ innate immune cells in rejection. *Nat Commun* **14**, (2023).
63. Shi, T. *et al.* Single-cell transcriptomic analysis of renal allograft rejection reveals insights into intragraft TCR clonality. *Journal of Clinical Investigation* **133**, (2023).
64. Hao, Y. *et al.* Integrated analysis of multimodal single-cell data. *bioRxiv* 2020.10.12.335331 (2020) doi:10.1101/2020.10.12.335331.
65. Stewart, B. J. *et al.* Spatio-temporal immune zonation of the human kidney Europe PMC Funders Group. **365**, 1461–1466 (2019).
66. Lake, B. B. *et al.* An atlas of healthy and injured cell states and niches in the human kidney. *Nature* **619**, 585–594 (2023).
67. Wigerblad, G. *et al.* Single-Cell Analysis Reveals the Range of Transcriptional States of Circulating Human Neutrophils. *The Journal of Immunology* **209**, 772–782 (2022).
68. Shankland, S. J., Smeets, B., Pippin, J. W. & Moeller, M. J. The emergence of the glomerular parietal epithelial cell. *Nature Reviews Nephrology* vol. 10 158–173 Preprint at https://doi.org/10.1038/nrneph.2014.1 (2014).
69. Tran, T. *et al.* In Vivo Developmental Trajectories of Human Podocyte Inform In Vitro Differentiation of Pluripotent Stem Cell-Derived Podocytes. *Dev Cell* **50**, 102-116.e6 (2019).
70. Schumacher, A. *et al.* Defining the variety of cell types in developing and adult human kidneys by single-cell RNA sequencing. *npj Regenerative Medicine* vol. 6 Preprint at https://doi.org/10.1038/s41536-021-00156-w (2021).
71. Varin, A. Alexis-Varin/RightSeuratTools: RightSeuratTools v1.0.1. Preprint at https://doi.org/10.5281/zenodo.12518909 (2024).
72. Thomas, G., Tacke, R., Hedrick, C. C. & Hanna, R. N. Nonclassical Patrolling Monocyte Function in the Vasculature. *Arterioscler Thromb Vasc Biol* **35**, 1306–1316 (2015).
73. Li, Z. *et al.* CD83: Activation marker for antigen presenting cells and its therapeutic potential. *Frontiers in Immunology* vol. 10 Preprint at https://doi.org/10.3389/fimmu.2019.01312 (2019).
74. Andreatta, M. & Carmona, S. J. UCell: Robust and scalable single-cell gene signature scoring. *Comput Struct Biotechnol J* **19**, 3796–3798 (2021).

75. Jin, S., Plikus, M. V & Nie, Q. CellChat for systematic analysis of cell-cell communication from single-cell and spatially resolved transcriptomics. *bioRxiv* 2023.11.05.565674 (2023) doi:10.1101/2023.11.05.565674.
76. van der Touw, W., Chen, H. M., Pan, P. Y. & Chen, S. H. LILRB receptor-mediated regulation of myeloid cell maturation and function. *Cancer Immunology, Immunotherapy* vol. 66 1079–1087 Preprint at https://doi.org/10.1007/s00262-017-2023-x (2017).
77. Redondo-García, S. *et al.* Human leukocyte immunoglobulin-like receptors in health and disease. *Frontiers in Immunology* vol. 14 Preprint at https://doi.org/10.3389/fimmu.2023.1282874 (2023).
78. Lakkis, F. G. & Li, X. C. Innate allorecognition by monocytic cells and its role in graft rejection. *American Journal of Transplantation* vol. 18 289–292 Preprint at https://doi.org/10.1111/ajt.14436 (2018).
79. Ennis, S., Ó Broin, P. & Szegezdi, E. CCPlotR: an R package for the visualization of cell–cell interactions. *Bioinformatics Advances* **3**, vbad130 (2023).
80. Street, K. *et al.* Slingshot: cell lineage and pseudotime inference for single-cell transcriptomics. *BMC Genomics* **19**, 477 (2018).
81. Van den Berge, K. *et al.* Trajectory-based differential expression analysis for single-cell sequencing data. *Nat Commun* **11**, (2020).
82. Taverna, F. *et al.* BIOMEX: an interactive workflow for (single cell) omics data interpretation and visualization. *Nucleic Acids Res* **48**, W385–W394 (2020).
83. Manel, N. *et al.* A cryptic sensor for HIV-1 activates antiviral innate immunity in dendritic cells. *Nature* **467**, 214–217 (2010).
84. Tinel, C. *et al.* Modulation of Monocyte Response by MicroRNA-15b/106a/374a During Antibody-mediated Rejection in Kidney Transplantation. *Transplantation* **107**, 1089–1101 (2023).
85. Van Gassen, S., Gaudilliere, B., Angst, M. S., Saeys, Y. & Aghaeepour, N. CytoNorm: A Normalization Algorithm for Cytometry Data. *Cytometry Part A* **97**, 268–278 (2020).
86. Fletez-Brant, K., Špidlen, J., Brinkman, R. R., Roederer, M. & Chattopadhyay, P. K. flowClean: Automated identification and removal of fluorescence anomalies in flow cytometry data. *Cytometry Part A* **89**, 461–471 (2016).
87. Vaulet, T. *et al.* Data-driven Derivation and Validation of Novel Phenotypes for Acute Kidney Transplant Rejection using Semi-supervised Clustering. *Journal of the American Society of Nephrology* **32**, 1084–1096 (2021).
88. Naesens, M., Cornell, L. D., Seshan, S. V. & Haas, M. Toward Activity and Chronicity Indices for the Evaluation of Kidney Transplant Rejection: A Viewpoint by the Banff Working Group. *Transplantation* (2025) doi:10.1097/TP.0000000000005336.

Acknowledgements

We thank the clinicians and surgeons, nursing staff and the patients of Dijon University Hospital. We thank Mickaël Ménager (Imagine Insitute, Paris) for providing the Vpx lentiviral vector. We thank Babacar Ndao (Inserm UMR Right, Besançon, France) for his help with fastq alignements. We thank Emilie Gaiffe, Caroline Laheurte and Eleonore Gravelin (Inserm UMR Right, Besançon, France) for their help with ORLY-EST samples. Figures 1a, 4a, 5a, 6a, 6g and 7 were created using Biorender.

Funding

MN is supported by the Research Foundation Flanders (F.W.O.) as senior clinical investigator (grant agreement no. 1844024N), and by a senior fundamental research project (grant agreement no. G038024N*)*. TV and MN are supported by the Research Council of the KU Leuven (grant agreement no. C2M24057). BL is supported by the Agence Nationale de la Recherche (grant JCJC n°ANR-22-CE18-0011-01). CT is supported by the Agence de la Biomédecine (grant Recherche et Greffe 2024) and the Bourgogne Franche-Comté region (grant RECH-ANER "Initials"). This research was financed by Inserm as part of the MESSIDORE 2024 call for projects operated by IReSP (grant AAP-2024-MSDR-367013).

Competing Interests Statement

The authors declare no conflict of interest regarding this manuscript.

Figure Legends

Figure 1.
a. Experimental Approach. 46 scRNA-Seq datasets from kidney transplant patients were used for this analysis (n = 13 blood with 5 no rejection and 8 rejection, and n = 33 kidney allograft biopsies with 13 no rejection and 20 rejection). b. Polar plot of the 28 rejection samples showing tissue origin and estimated inflammation level severity. c. Clustered dots plot showing average gene expression values of canonical markers (log normalized) and expression percentage of cell types represented on the Uniform Manifold Approximation and Projection (UMAP) plot. d. UMAP plot of 150,876 cells passing QC filtering and doublets removal. The main kidney cell types are represented, including loop of Henle (LOH), podocytes, vascular smooth muscle and pericytes (vSMp), proximal tubule (PT), intercalated cells type A and B (IC_A / IC_B), three endothelial cell subsets comprising vasa recta (ECvr), glomerular (ECg) and peritubular capillaries (ECptc), myeloid cells, lymphoid cells, megakaryocytes, and proliferating cells. e. Stacked barplots representing the relative cell proportion of each cell type on the UMAP plot, split by tissue origin (blood or kidney allograft biopsies) and by outcome (no rejection or rejection).

Figure 2.
a. UMAP plot of 37,847 cells following Seurat's reintegration of monocytes, macrophages and cDC cell types from the main object. The main myeloid cell types are represented, including the three expected subsets of monocytes (Classical-mo, Intermediate-mo and Non-classical-mo) as well as more specific subtypes such as classical monocytes activated by interferon-gamma (IFN-activated-mo), classical monocytes in the process of differentiating into monocyte-derived dendritic cells (Mo-DC), and non-classical monocytes expressing higher levels of adhesion molecules (Patrolling-mo). Three subtypes of dendritic cells were also found, with both expected main conventional subsets (cDC1 and cDC2) and a *CD14*+ *CD83*+ cluster of monocyte-derived mature dendritic cells (*CD83*+ mature DC). Finally, two macrophages subtypes were identified, one expressing high levels of *SELENOP* (*SELENOP*+) and another expressing high levels of several chemokines (*CXCL10*+). b. Clustered dots plot showing average gene expression values of canonical markers (log normalized) and expression percentage of major cell types represented on the UMAP plot. c. Stacked barplots representing the relative cell proportion of each myeloid cell type among all kidney allograft cells, split by outcome (no rejection or rejection). d. Scatterplot representing the relative proportion ratio of each myeloid cell type

among all kidney allograft cells in no rejection versus rejection samples, defining an infiltration score for each myeloid cell type during rejection. e. Barplots showing the relative proportion of *SELENOP*+ and *CXCL10*+ macrophages among all myeloid cells in no rejection versus rejection samples. Two-tailed Mann–Whitney tests comparing No rejection and Rejection samples indicate significant difference in *CXCL10*+ macrophages proportions but not in *SELENOP*+ macrophages proportions. Two-tailed Mann Whitney tests were performed to compare the groups. P-values are shown. f. Volcano plot representing DEG between *SELENOP*+ and *CXCL10*+ macrophages.

Figure 3:
a. UMAP plots of reintegrated myeloid cells showing the 6 unsupervised trajectories obtained from slingshot and represented on cell type annotations and tissue origin, as well as pseudotime values corresponding to these trajectories and knots determined by tradeSeq and segmenting each lineage. b. Scatterplots representing early DE test between knot 3 and 4 computed statistics (Wald statistic, mean log fold change and rank score for each gene) of fitted GAM expression smoothers in 5 within-lineage comparisons (*CD83*+ DC trajectory versus *CXCL10*+ trajectory, cDC1 trajectory versus *CXCL10*+ trajectory, *SELENOP*+ trajectory versus *CXCL10*+ trajectory, Non-classical trajectory versus *CXCL10*+ trajectory and Patrolling trajectory versus *CXCL10*+ trajectory). c. Venn diagram showing overlapping genes among the top 90th percentile rank score in each of the 5 within-lineage comparisons of the CXCL10+ macrophages trajectory versus each other trajectory. d. Heatmap of the fitted GAM expression smoothers of 22 genes found to be significantly enriched in all 5 within-lineage comparisons of the *CXCL10*+ macrophages trajectory versus each other trajectory, shown alongside the pseudotime of the *CXCL10*+ macrophages lineage. Density of each cell type contributing to the trajectory is shown.
e. Scatterplots of the log normalized expression and the corresponding fitted GAM expression smoothers curves of 6 significantly enriched genes in all 5 within-lineage comparisons of the *CXCL10*+ macrophages trajectory versus each other trajectory, represented alongside the pseudotime of all 6 identified lineages.

Figure 4:
a. Eighty four patients were included in the ORLY EST multicenter cohort. PBMC and serum were collected at D0 and D365 post-transplant and stored at the CRB and the histocompatibility laboratory of Dijon University Hospital respectively. The proposed study is an ancillary study based on flow cytometric analysis of LILR expression in leukocytes. b. Normalized Expression of indicated markers at indicated times in indicated monocyte population. Multiple paired t tests were performed using Holm-Šídák method to compare the groups. P-values are shown.

Figure 5: a. Schematic diagram of the experiments. b Representative overlays histograms representing the expression of annotated markers in different stimulatory conditions. c. Geometric Mean MFI of each biological replicate (N=10). Wilcoxon matched-pairs signed rank tests were used and P-values are shown.

Figure 6: a. Schematic diagram of the lentiviral strategy used here. b. Gating strategy showing the efficacy of the approach. c. Percent of LILRB2 hi macrophages after transduction. Two-tailed Mann Whitney test was performed to compare the groups. P-values is shown. d. Gating strategy for HLA binding assays. e-f Percentages of HLA-A2 or B-27 cells. Two-tailed Mann Whitney tests were performed to compare the groups. P-values are shown. g. Schematic diagram of CD3-CD28 activated autologous T cell proliferation assay upon co-culture with LILRB2 hi macrophages. h-i. Division index of the activated T cell post co culture with LILRB2 hi macrophages. Wilcoxon matched-pairs signed rank tests were performed to compare the NT and LILRB2hi conditions. P-values are shown.

Figure 7: Mechanism of activation of kidney transplant recipient-derived monocytes in the context of kidney transplantation. The upper part of the figure suggests that in a context of balanced signals provided by CD47 and SIRPa, recipient-derived monocytes transform into SELENOP+ resident macrophages. In contrast, in the presence of an imbalanced CD47/SIRPA situation, monocytes transform into inflammatory macrophages expressing LILRB2 and CXCL10 or into memory monocytes overexpressing LILRB2.

Fig.1

a.

N=46 scRNA-Seq datasets from kidney transplant recipients
N=13 Blood
(N=5 No Rejection and N=8 Rejection)

N=33 Kidney allograft
(N=13 No Rejection and N=20 Rejection)

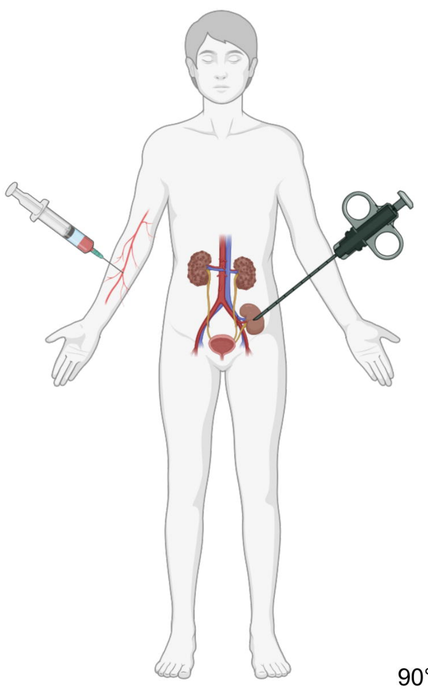

b.

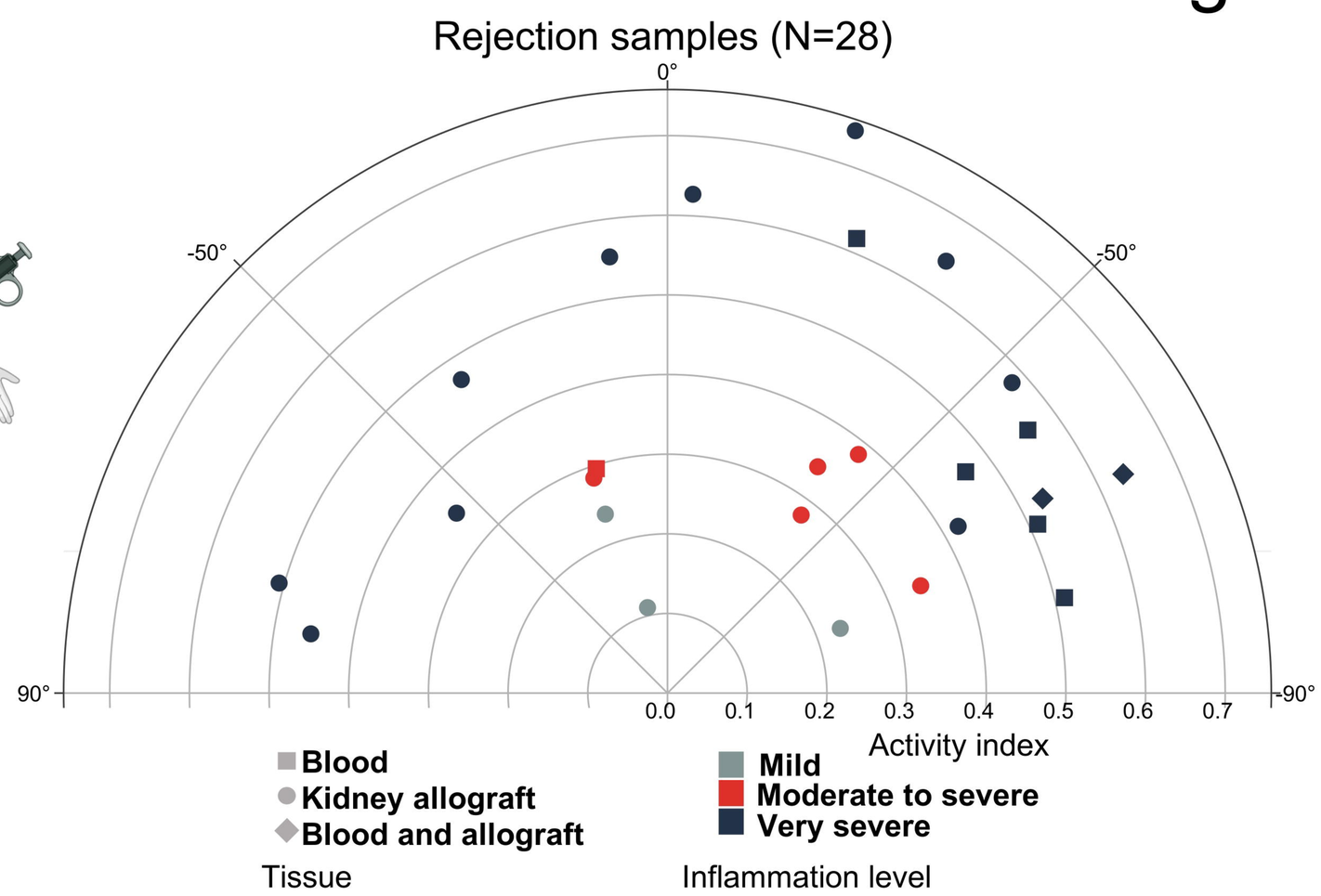

c.

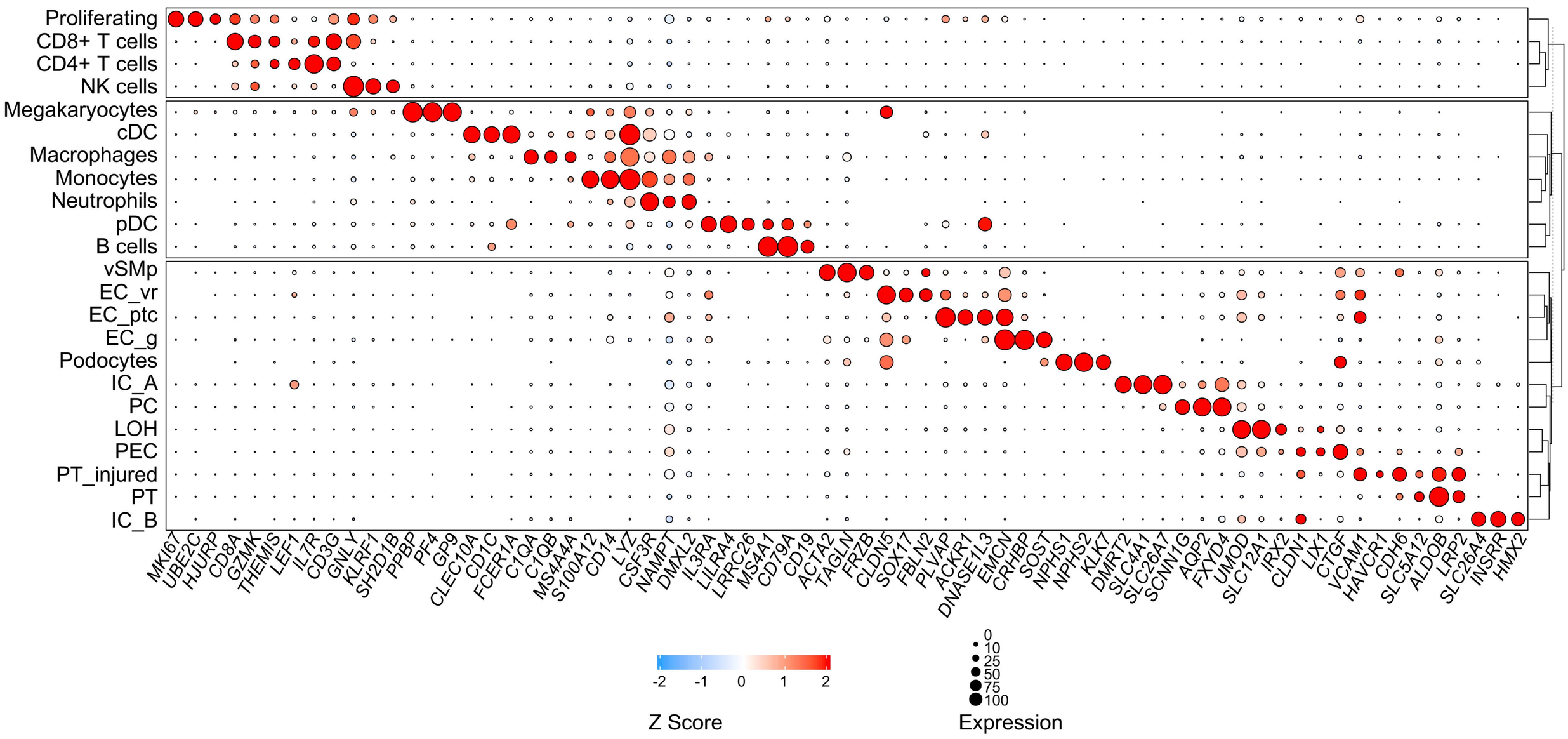

d.

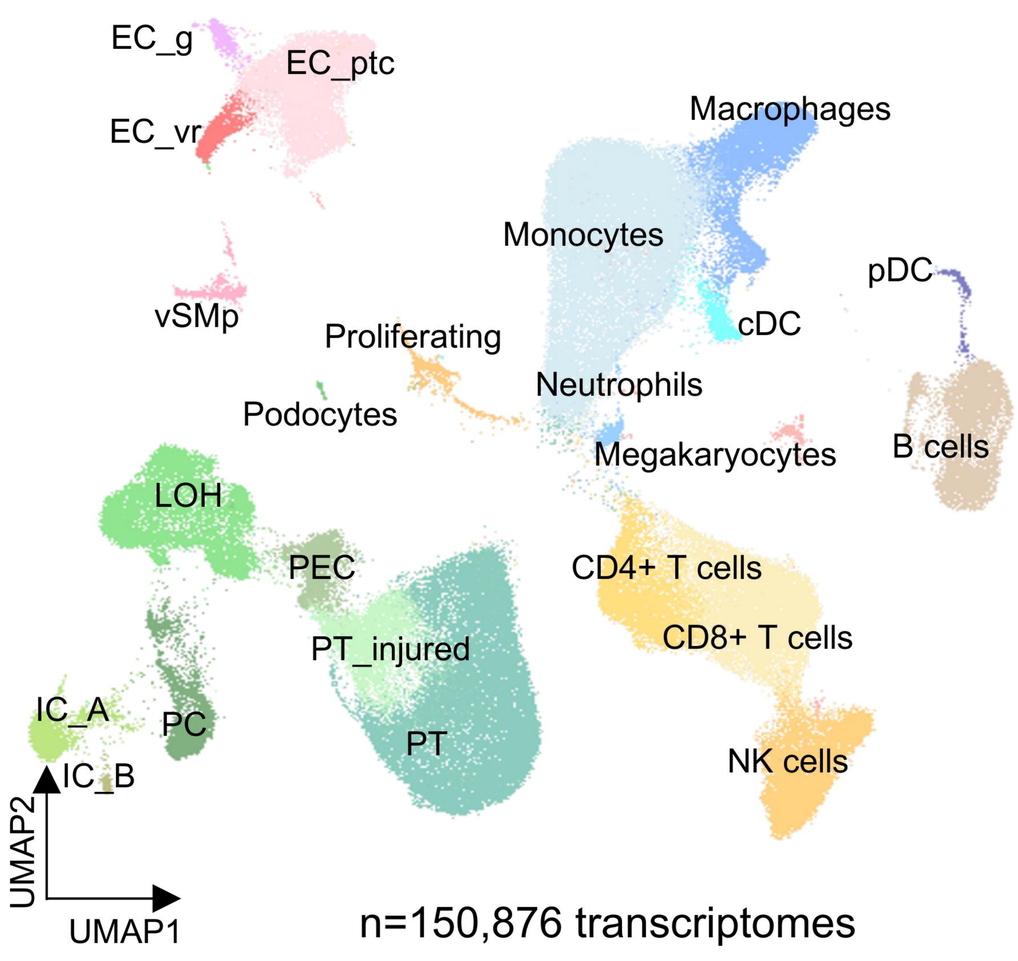

e.

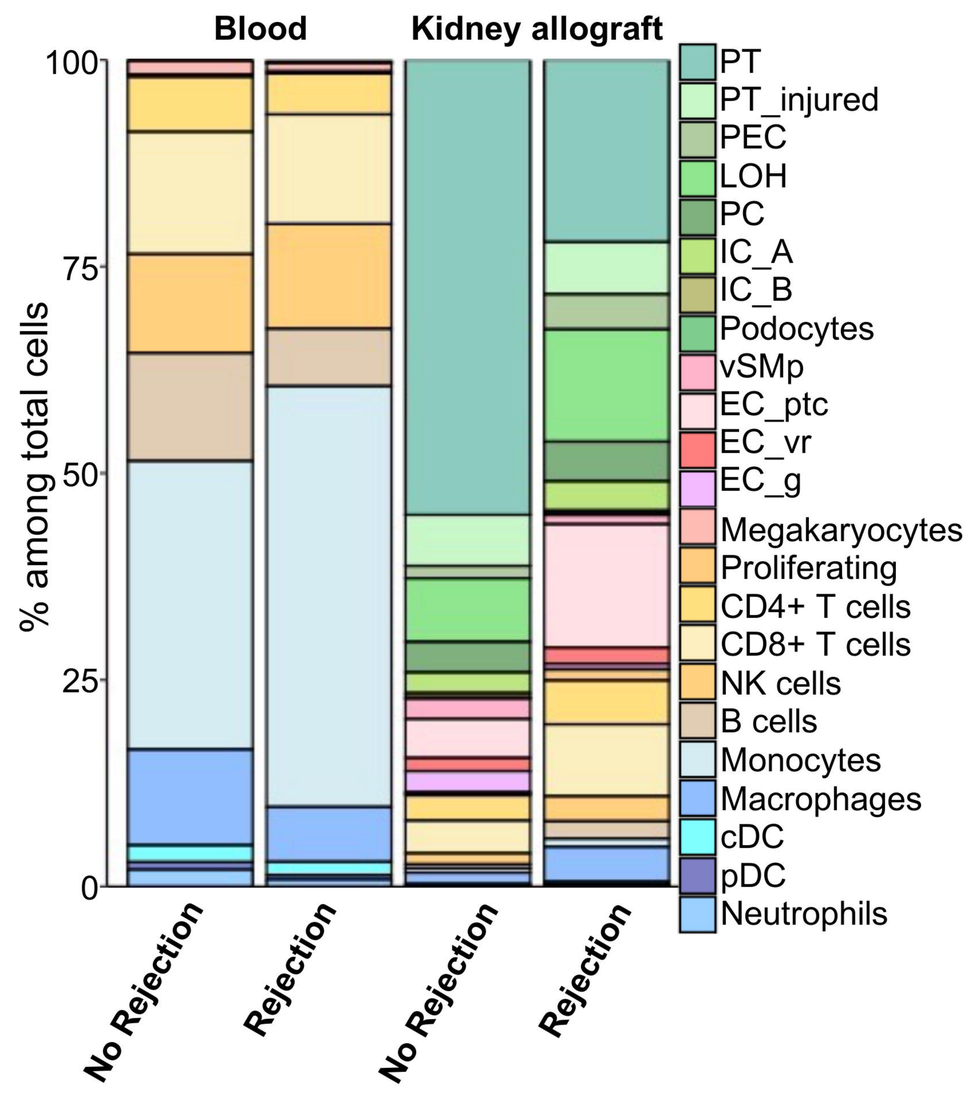

f.

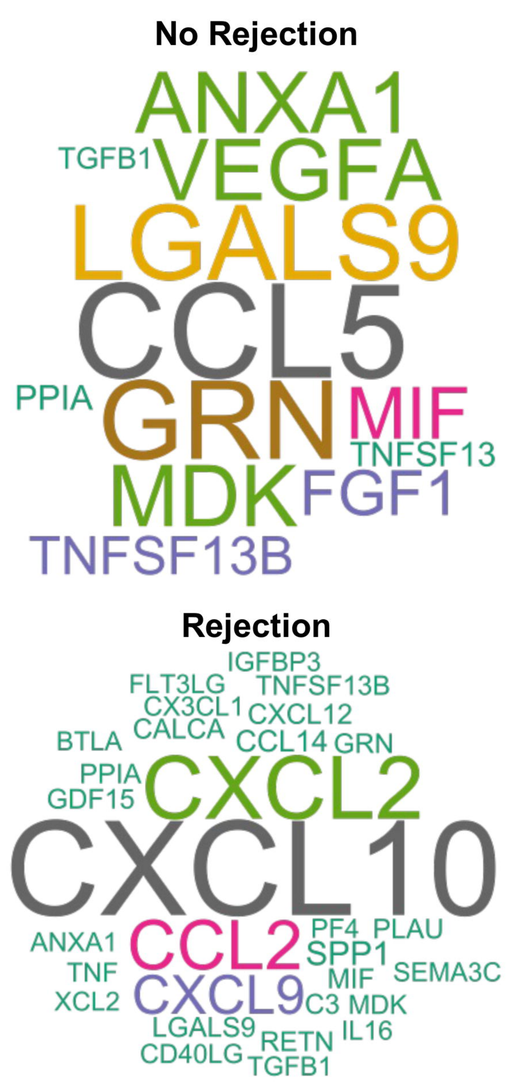

Fig.2

a.

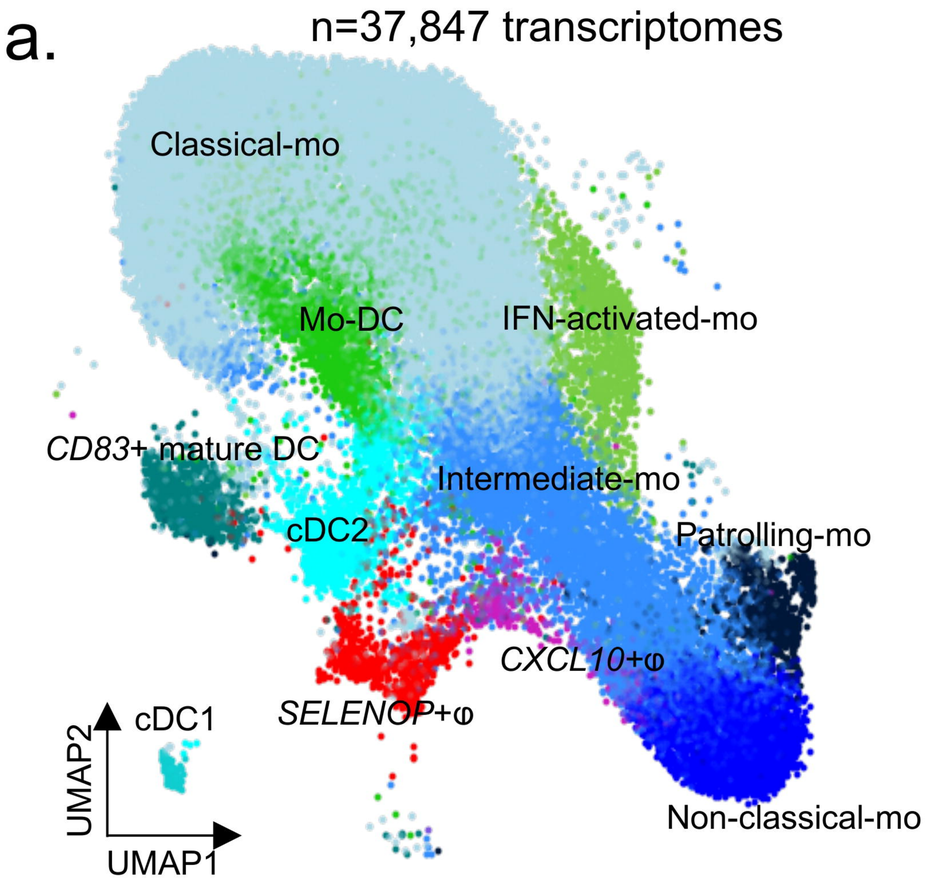
n=37,847 transcriptomes
Classical-mo
Mo-DC
IFN-activated-mo
CD83+ mature DC
Intermediate-mo
cDC2
Patrolling-mo
CXCL10+φ
SELENOP+φ
cDC1
Non-classical-mo
UMAP2
UMAP1

b.

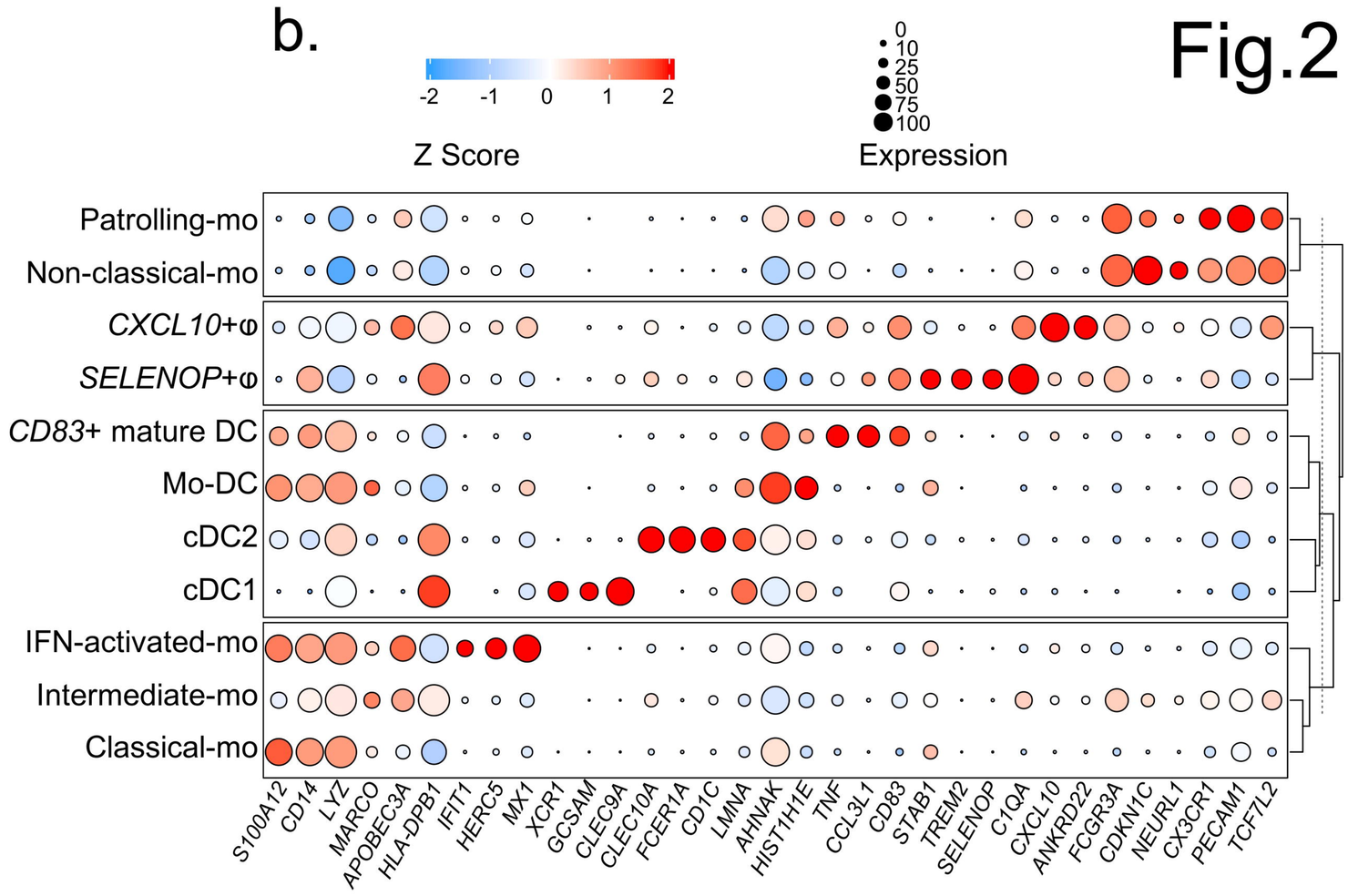
Z Score
-2 -1 0 1 2
Expression
0 10 25 50 75 100
Patrolling-mo
Non-classical-mo
CXCL10+φ
SELENOP+φ
CD83+ mature DC
Mo-DC
cDC2
cDC1
IFN-activated-mo
Intermediate-mo
Classical-mo
S100A12 CD14 LYZ MARCO APOBEC3A HLA-DPB1 IFIT1 HERC5 MX1 XCR1 GCSAM CLEC9A CLEC10A FCER1A CD1C LMNA AHNAK HIST1H1E TNF CCL3L1 CD83 STAB1 TREM2 SELENOP C1QA CXCL10 ANKRD22 FCGR3A CDKN1C NEURL1 CX3CR1 PECAM1 TCF7L2

c.

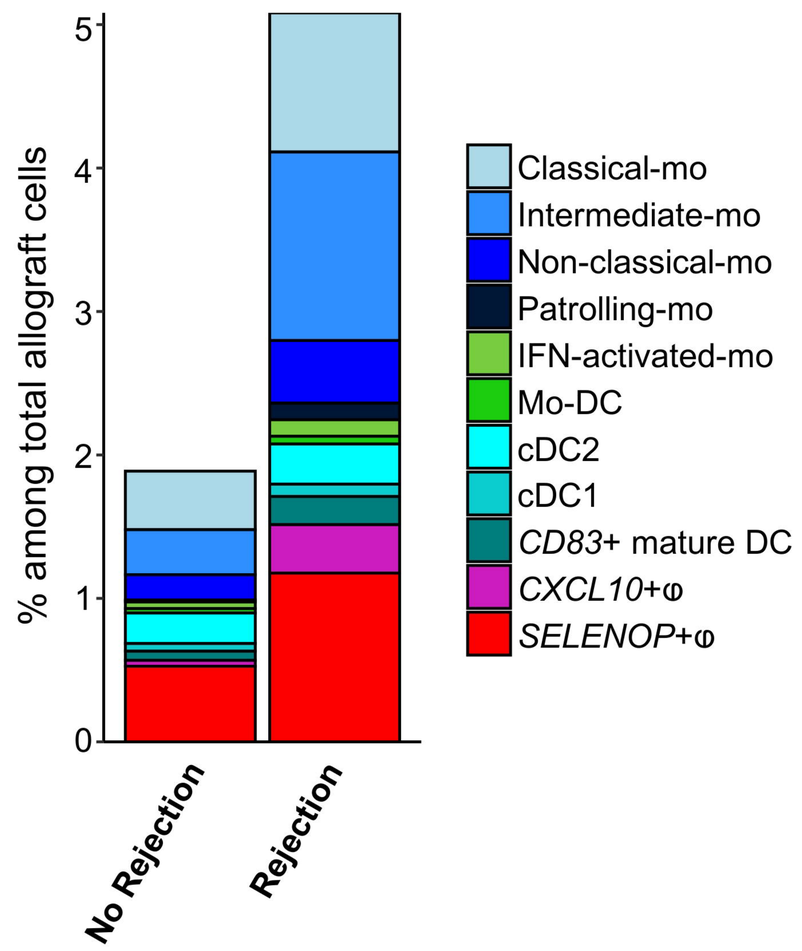
% among total allograft cells
No Rejection
Rejection
Classical-mo
Intermediate-mo
Non-classical-mo
Patrolling-mo
IFN-activated-mo
Mo-DC
cDC2
cDC1
CD83+ mature DC
CXCL10+φ
SELENOP+φ

d.

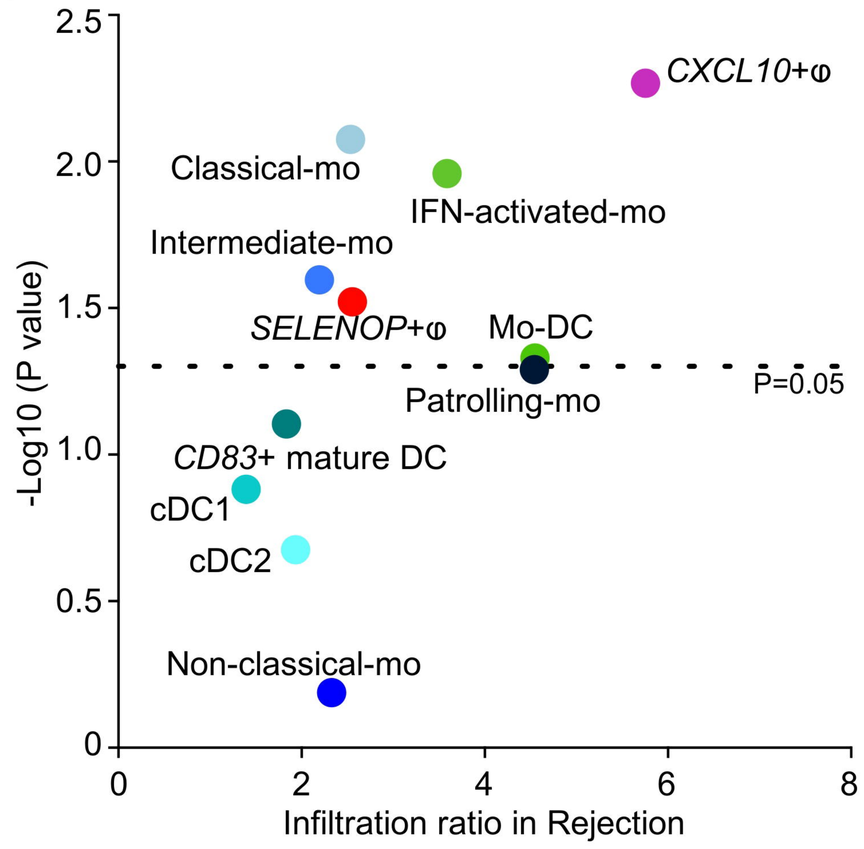
-Log10 (P value)
Infiltration ratio in Rejection
CXCL10+φ
Classical-mo
IFN-activated-mo
Intermediate-mo
SELENOP+φ
Mo-DC
Patrolling-mo
P=0.05
CD83+ mature DC
cDC1
cDC2
Non-classical-mo

e.

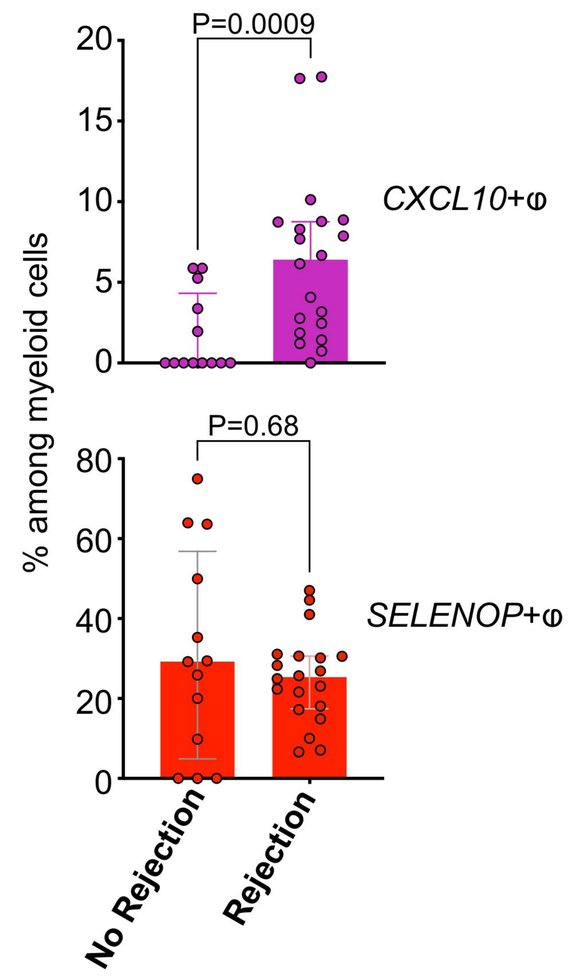
% among myeloid cells
P=0.0009
CXCL10+φ
P=0.68
SELENOP+φ
No Rejection
Rejection

f.

Upregulated in CXCL10+φ
N=112 DEG
Upregulated in SELENOP+φ
N=56 DEG
Log2 Fold Change (CXCL10+φ vs SELENOP-φ)
-Log10 (P adj value)
CXCL10
WARS
GBP1
S100A4
LILRB1
CXCL9
ANKRD22
S100A6
GBP2
GBP5
CD52
IFITM3
GBP4
LY6E
LILRA2
LILRA1
LILRB2
LILRA5
CD81
C1QC
AKR1B1
RNASE1
STAB1
A2M
ALOX5AP
C3
GPR34
SLC40A1
APOC1
APOE
TREM2
GPNMB
ADAM28
SELENOP

Fig.3

a.

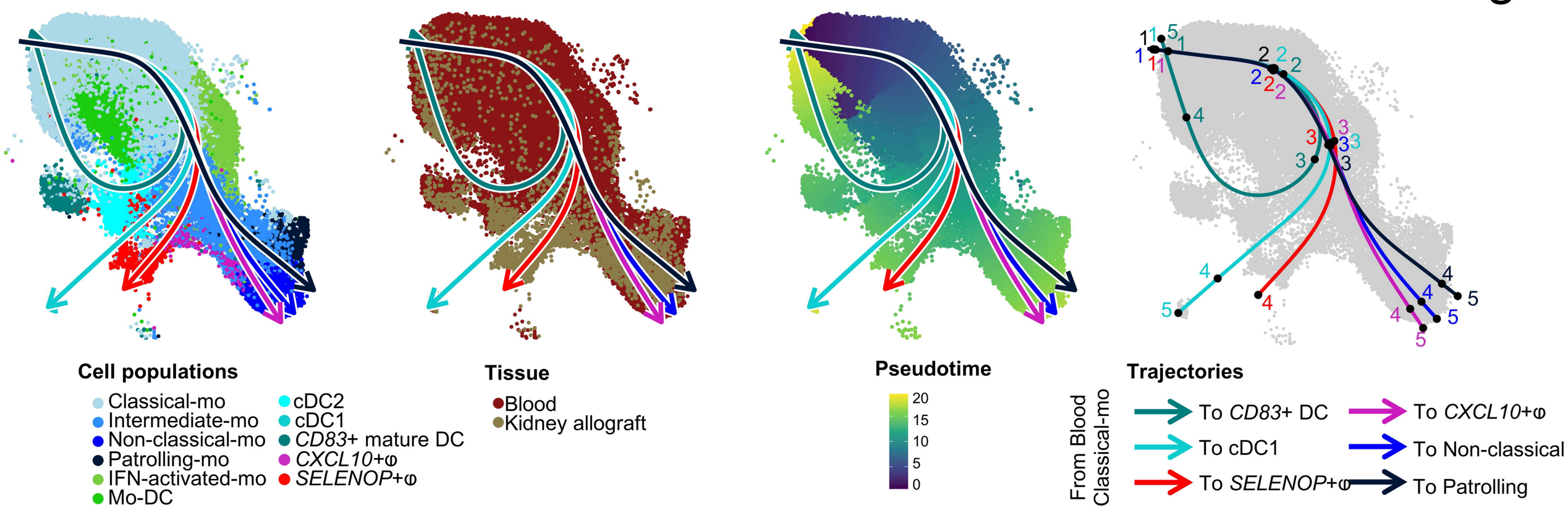
Cell populations
Classical-mo
Intermediate-mo
Non-classical-mo
Patrolling-mo
IFN-activated-mo
Mo-DC
cDC2
cDC1
CD83+ mature DC
CXCL10+φ
SELENOP+φ
Tissue
Blood
Kidney allograft
Pseudotime
20
15
10
5
0
Trajectories
From Blood Classical-mo
To CD83+ DC
To cDC1
To SELENOP+φ
To CXCL10+φ
To Non-classical
To Patrolling

b.

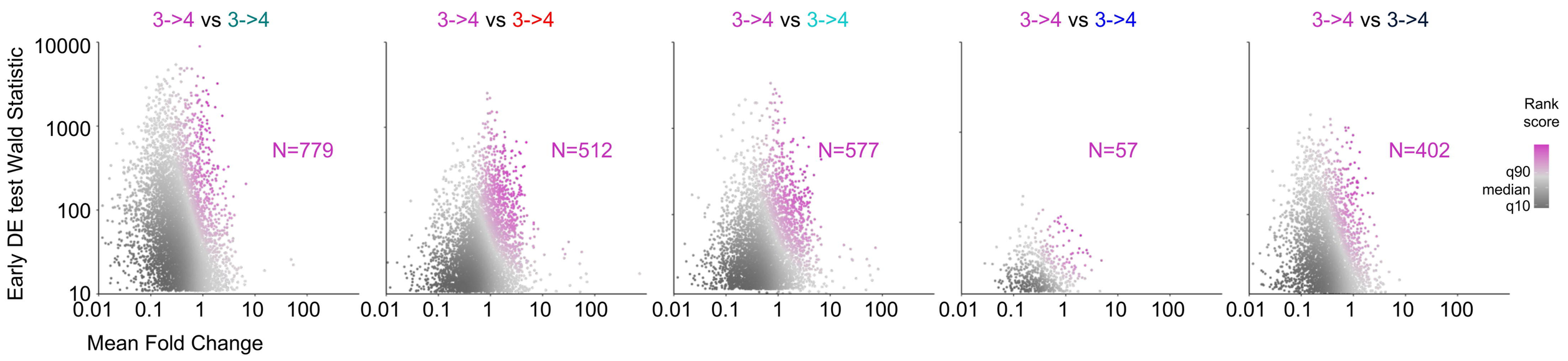
3->4 vs 3->4
N=779
N=512
N=577
N=57
N=402
Early DE test Wald Statistic
Mean Fold Change
Rank score
q90
median
q10

c.

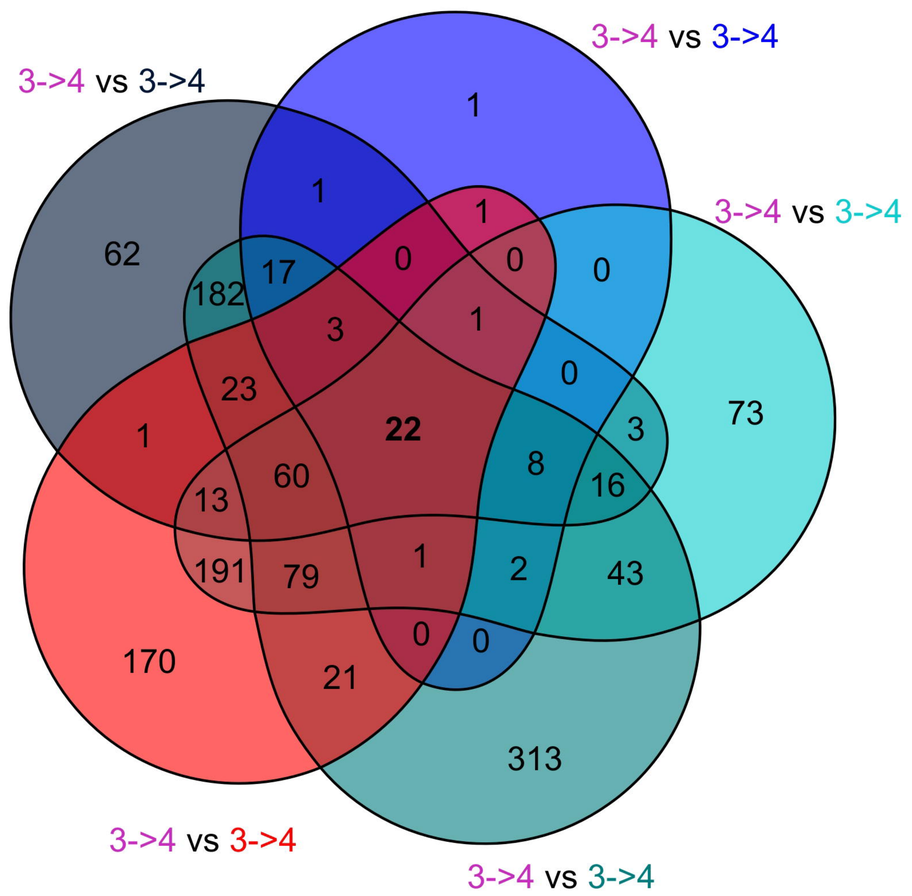
3->4 vs 3->4
3->4 vs 3->4
3->4 vs 3->4
3->4 vs 3->4
3->4 vs 3->4
62
182
17
1
1
1
0
0
0
3
1
23
22
1
0
3
73
13
60
8
16
191
79
1
2
43
170
21
0
0
313

d.

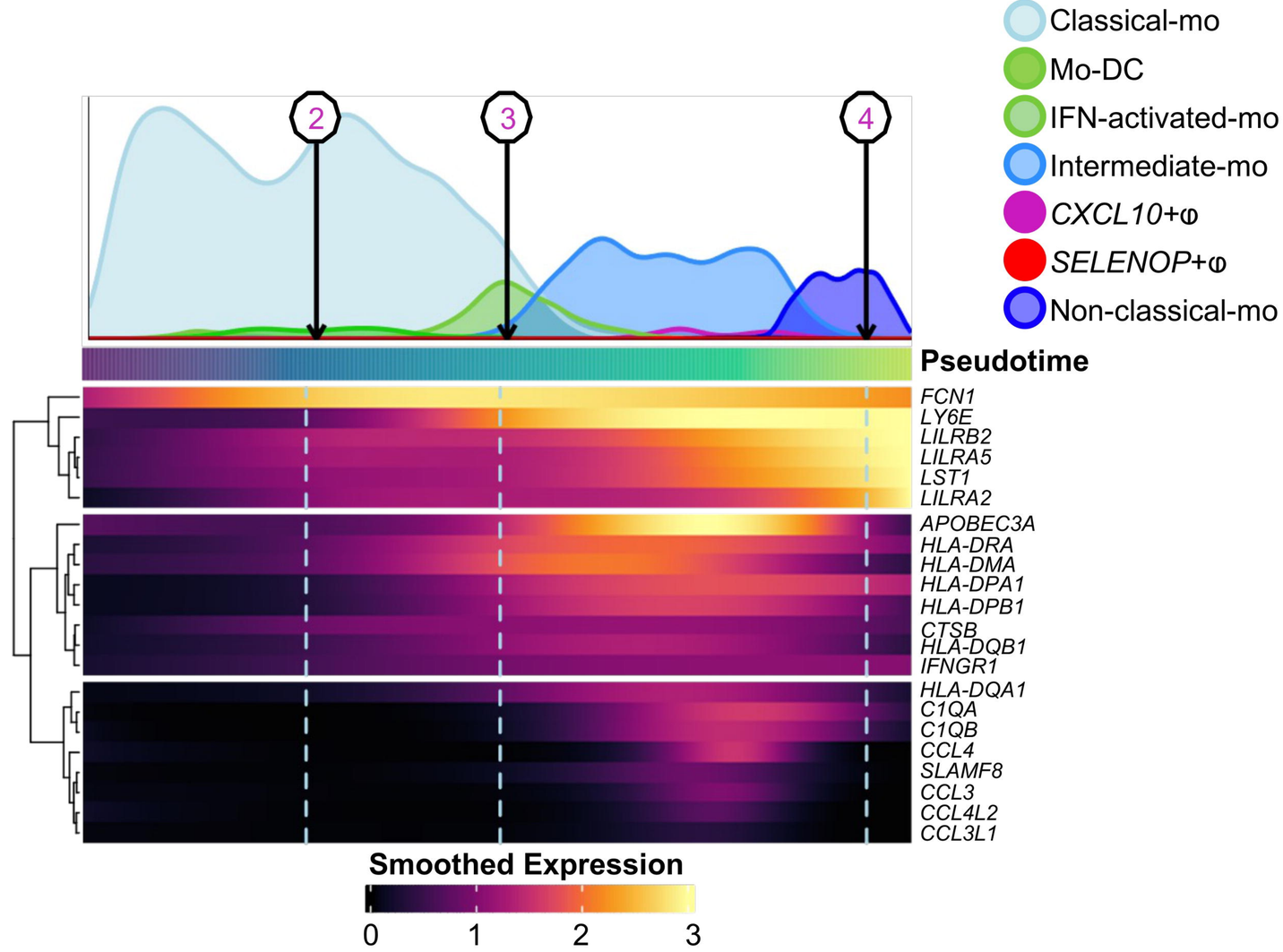
Classical-mo
Mo-DC
IFN-activated-mo
Intermediate-mo
CXCL10+φ
SELENOP+φ
Non-classical-mo
Pseudotime
FCN1
LY6E
LILRB2
LILRA5
LST1
LILRA2
APOBEC3A
HLA-DRA
HLA-DMA
HLA-DPA1
HLA-DPB1
CTSB
HLA-DQB1
IFNGR1
HLA-DQA1
C1QA
C1QB
CCL4
SLAMF8
CCL3
CCL4L2
CCL3L1
Smoothed Expression

e.

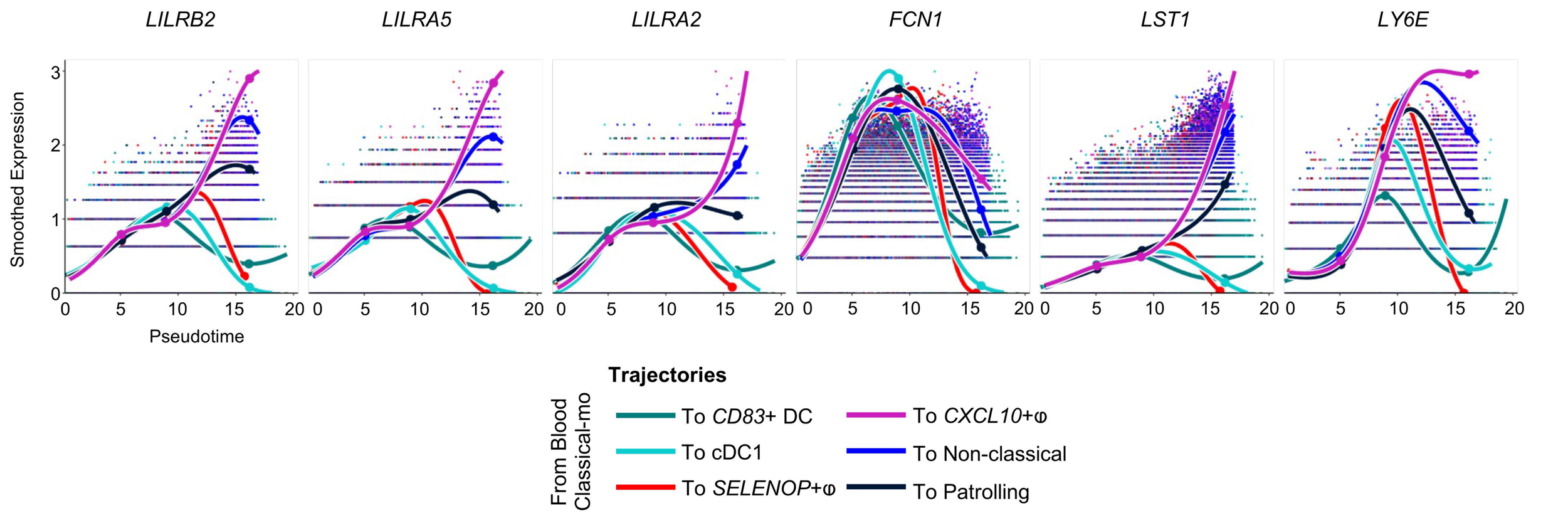
LILRB2
LILRA5
LILRA2
FCN1
LST1
LY6E
Smoothed Expression
Pseudotime
Trajectories
From Blood Classical-mo
To CD83+ DC
To cDC1
To SELENOP+φ
To CXCL10+φ
To Non-classical
To Patrolling

Fig.4

a.

N=64 kidney transplant recipients
(N=56 No Rejection and N=8 Rejection)

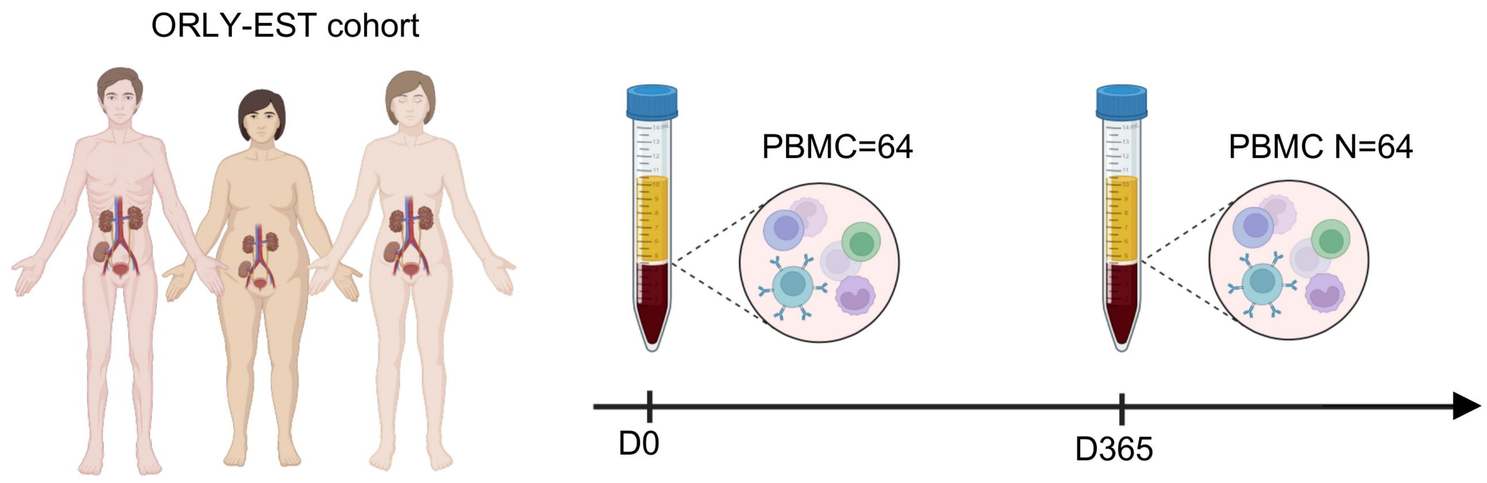

b.

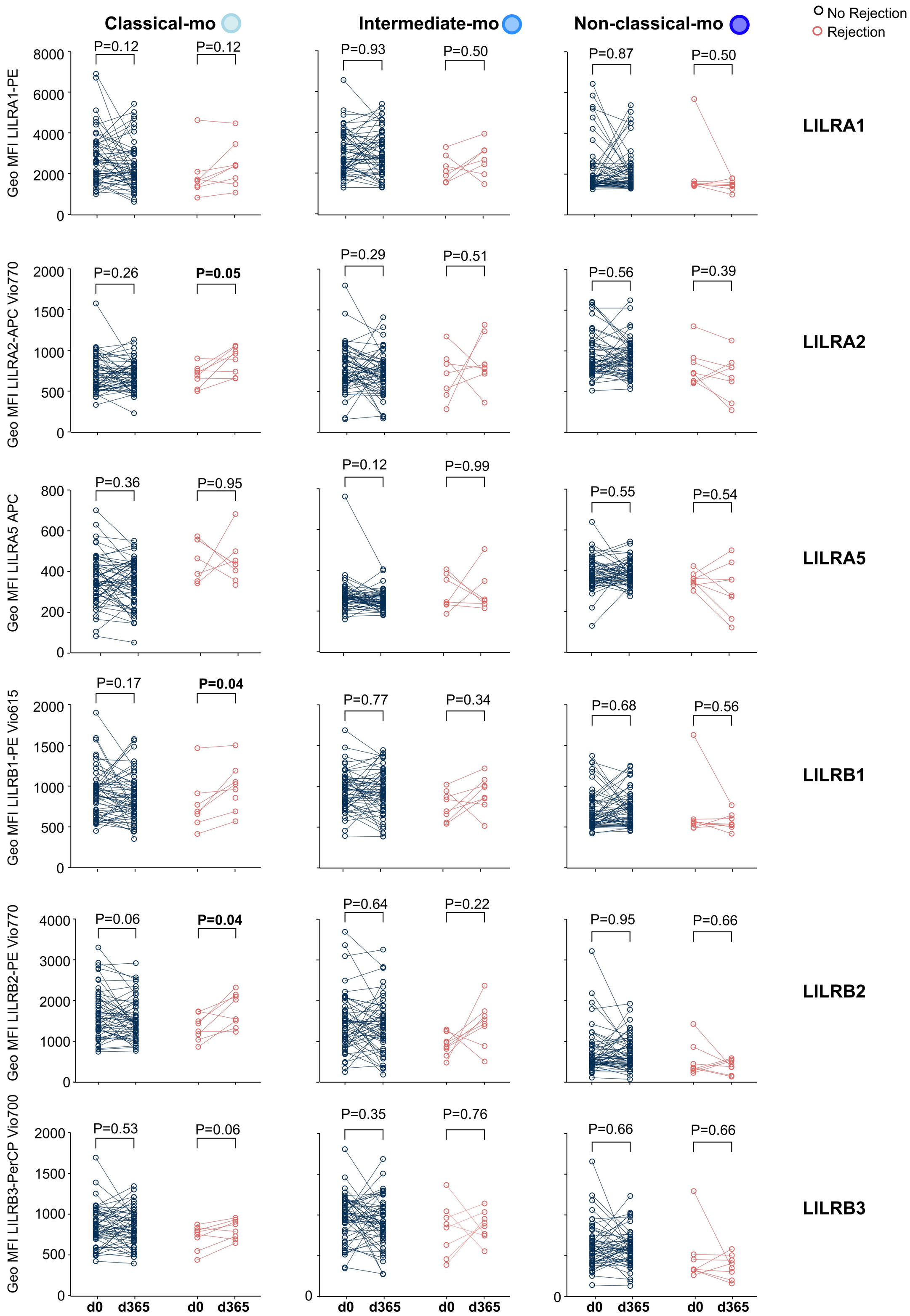

Fig.5

a.

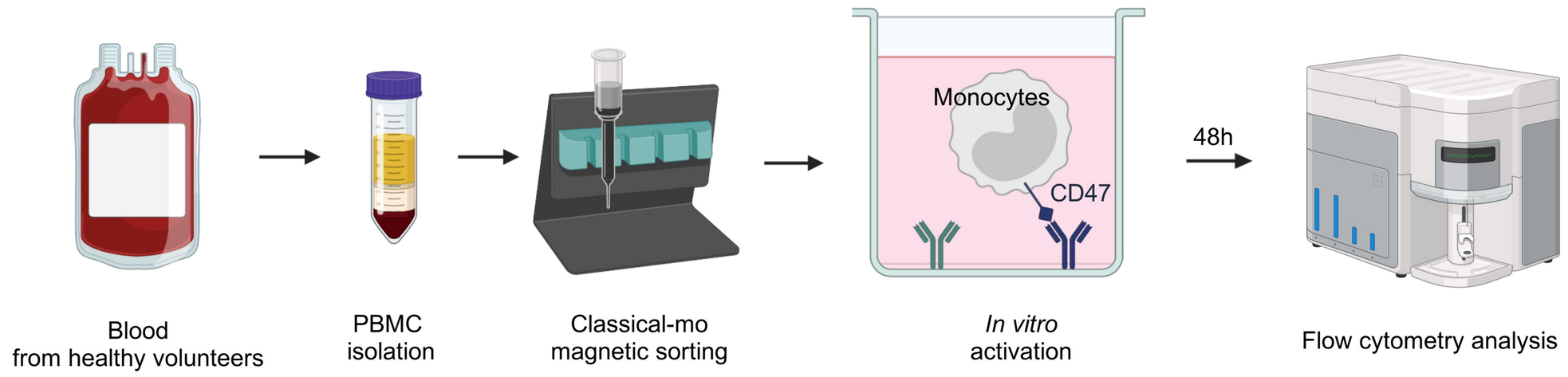
Monocytes
CD47
48h
Blood
from healthy volunteers
PBMC
isolation
Classical-mo
magnetic sorting
In vitro
activation
Flow cytometry analysis

b.

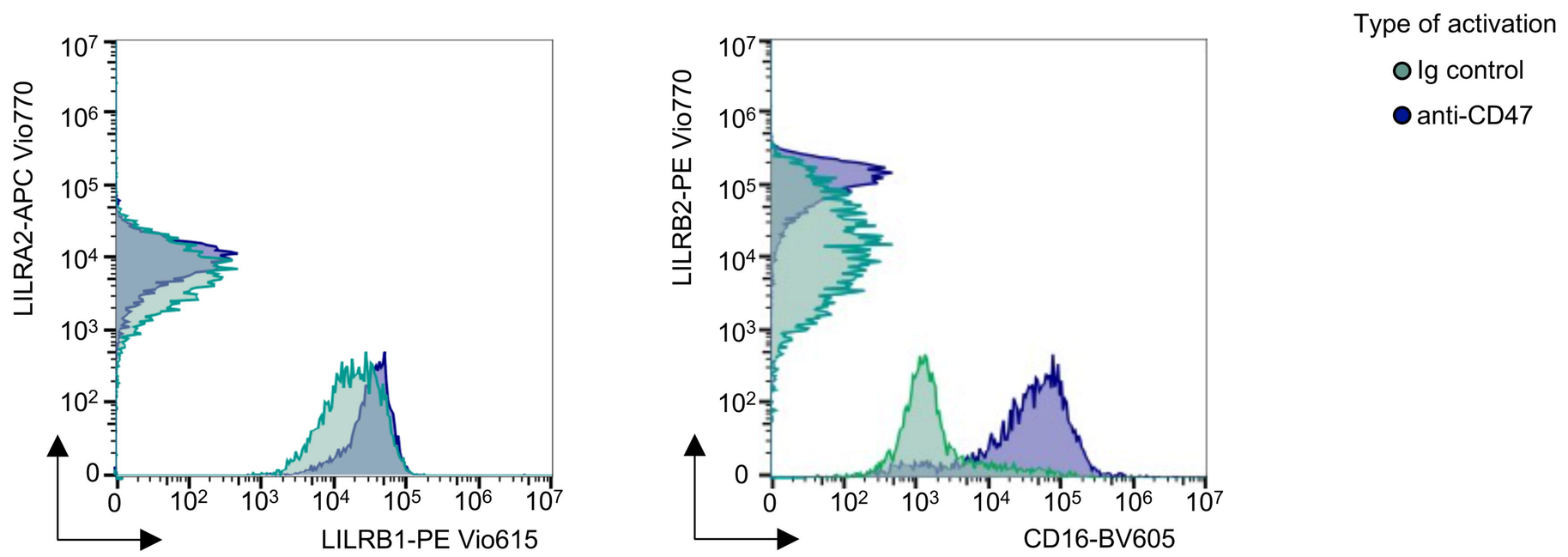
LILRA2-APC Vio770
LILRB1-PE Vio615
LILRB2-PE Vio770
CD16-BV605
Type of activation
Ig control
anti-CD47

c.

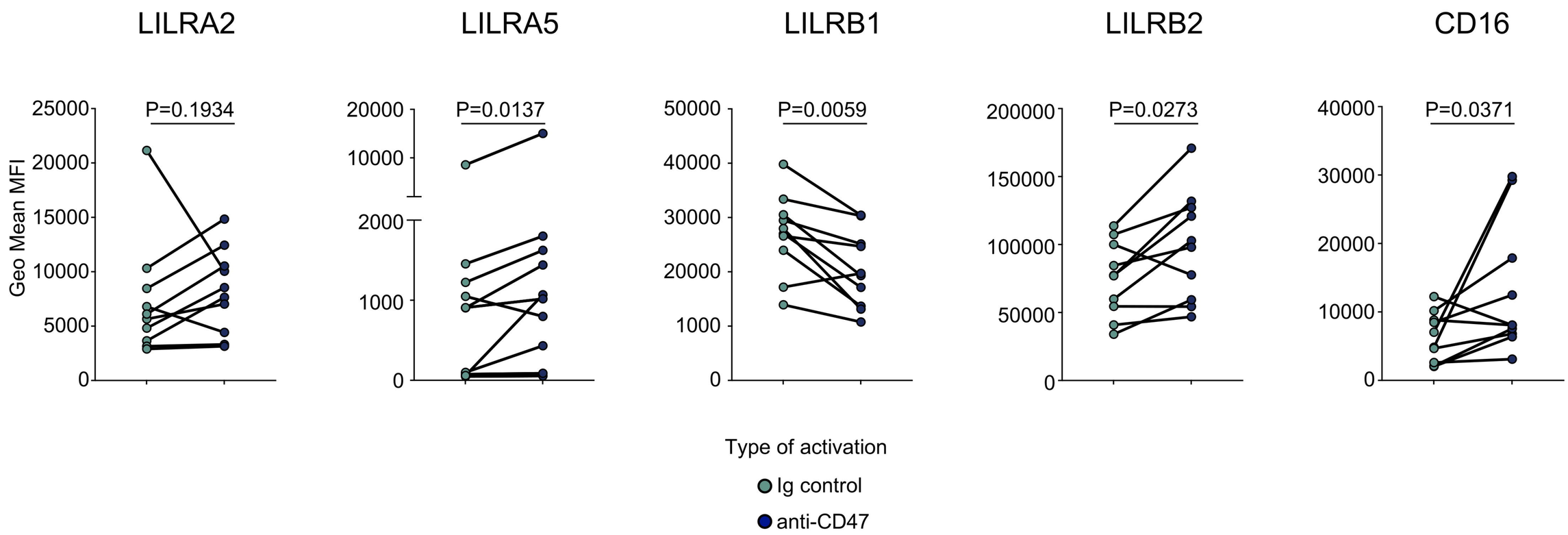
LILRA2
LILRA5
LILRB1
LILRB2
CD16
Geo Mean MFI
P=0.1934
P=0.0137
P=0.0059
P=0.0273
P=0.0371
Type of activation
Ig control
anti-CD47

Fig.6

a.

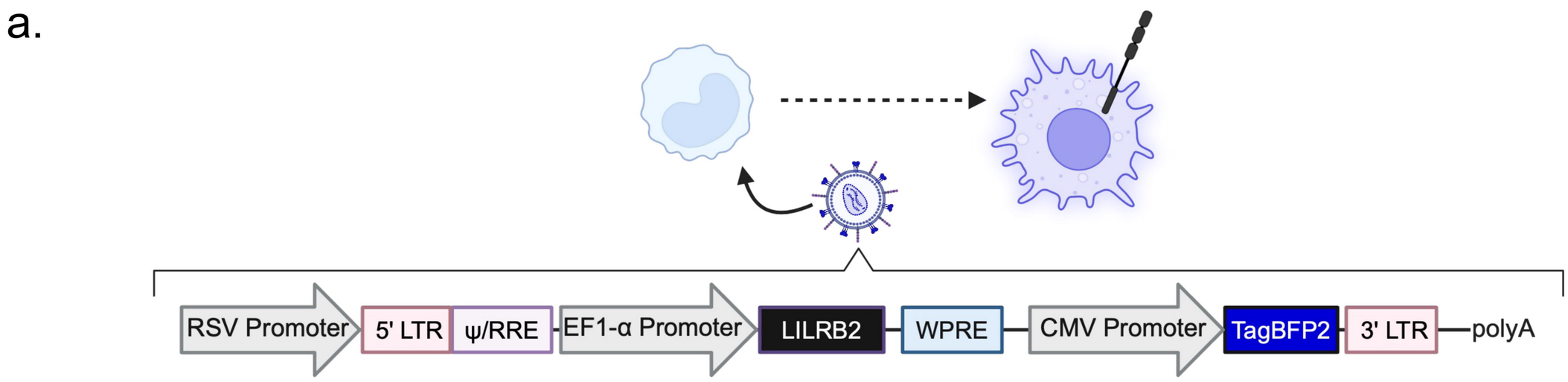

b.

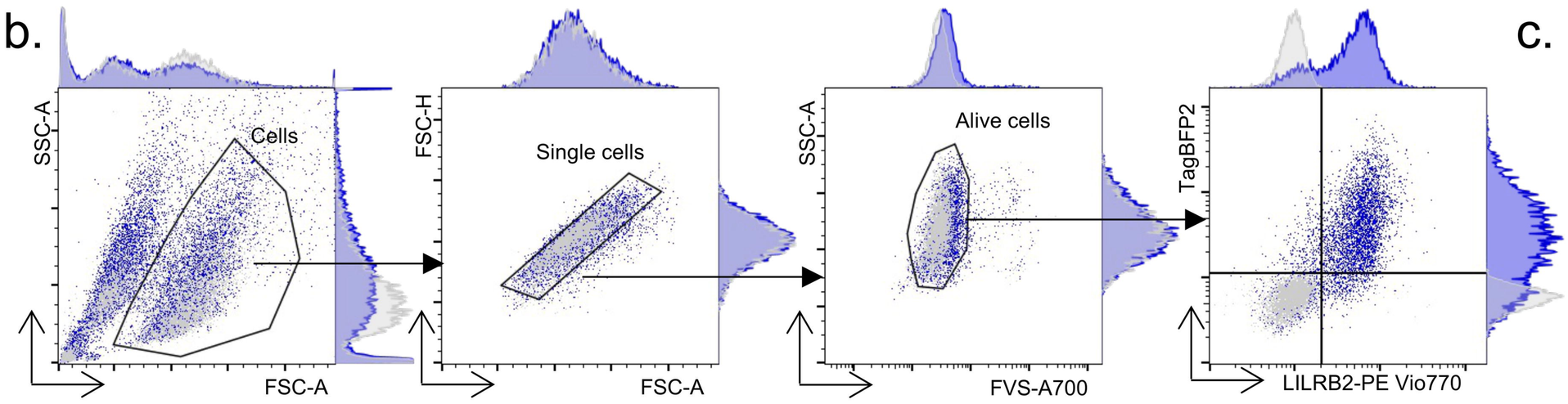

c.

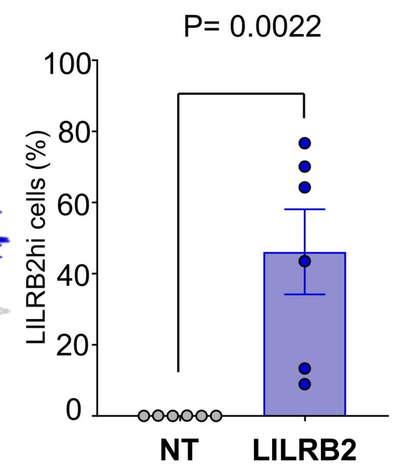

d.

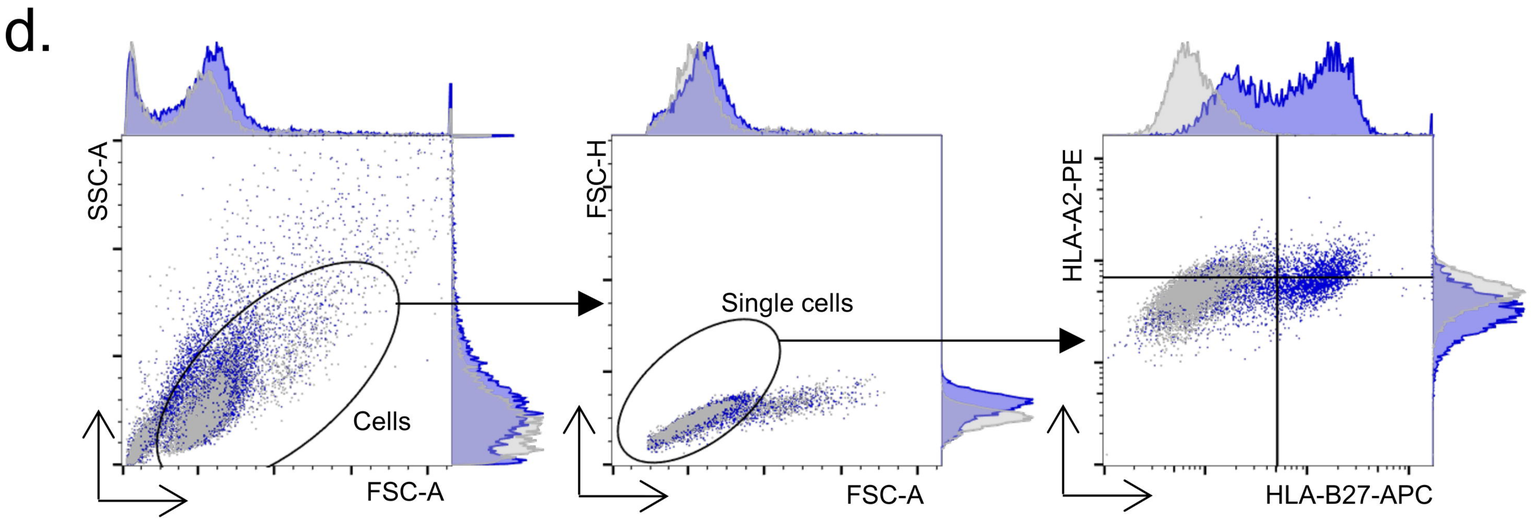

e.

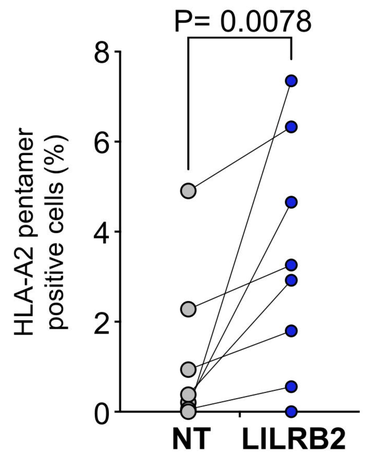

f.

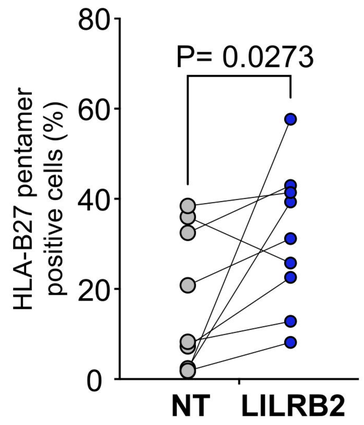

g.

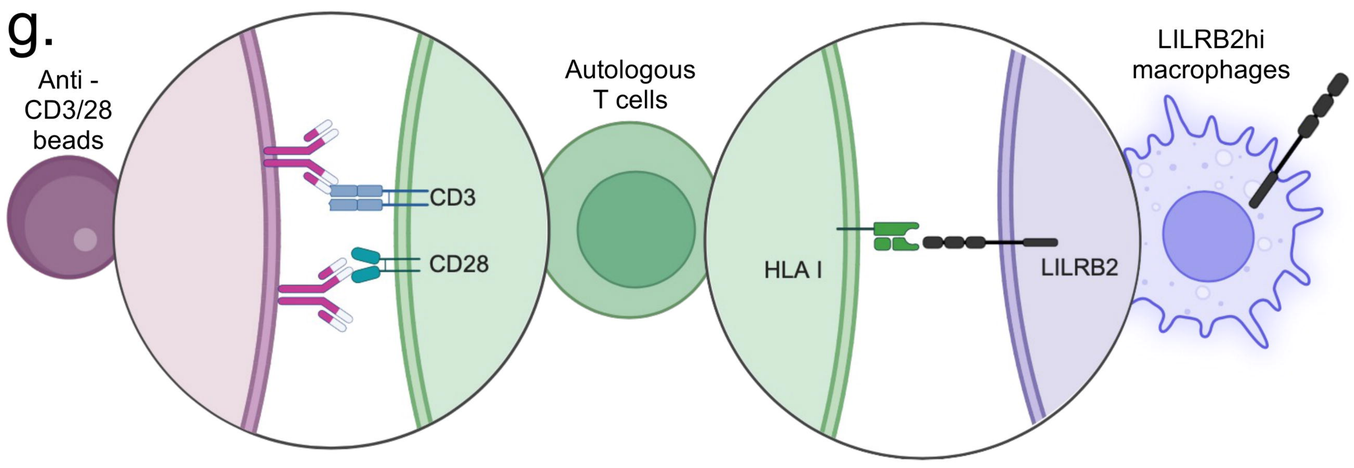

h.

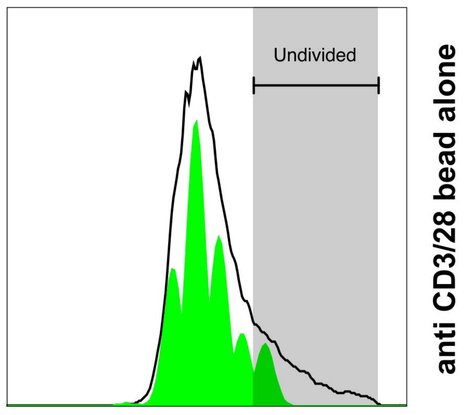

i.

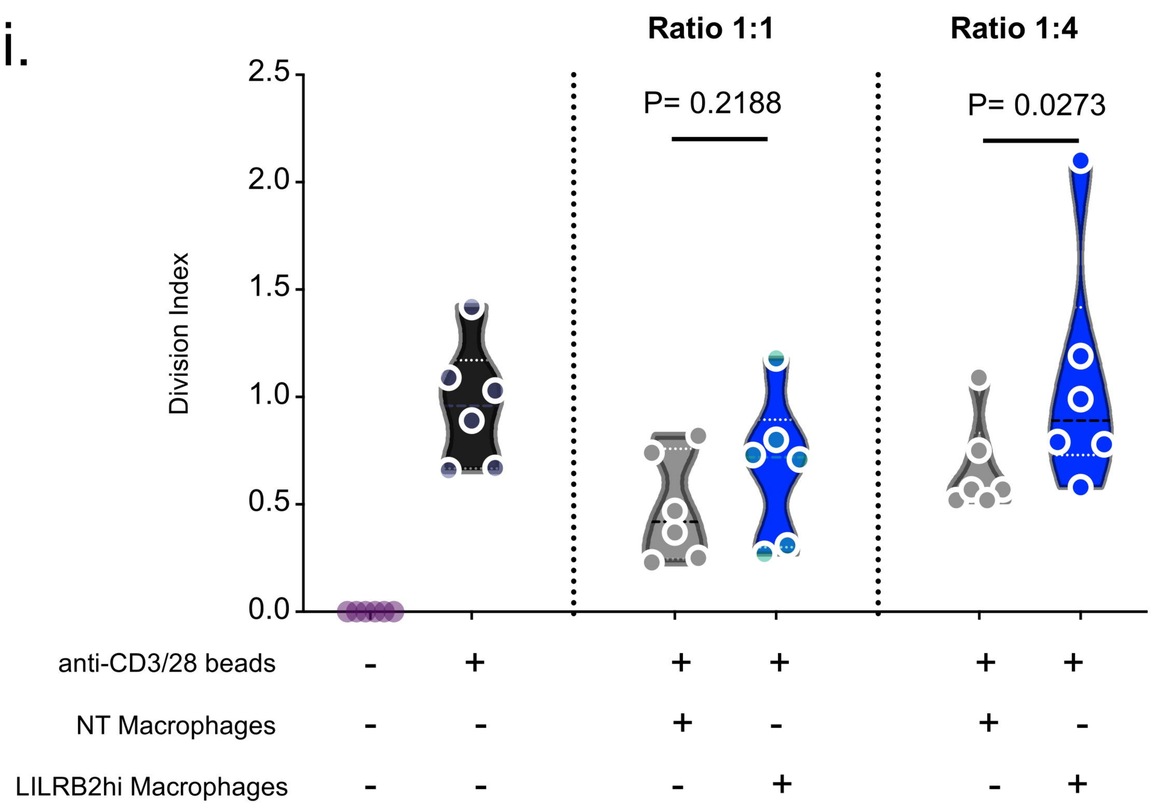

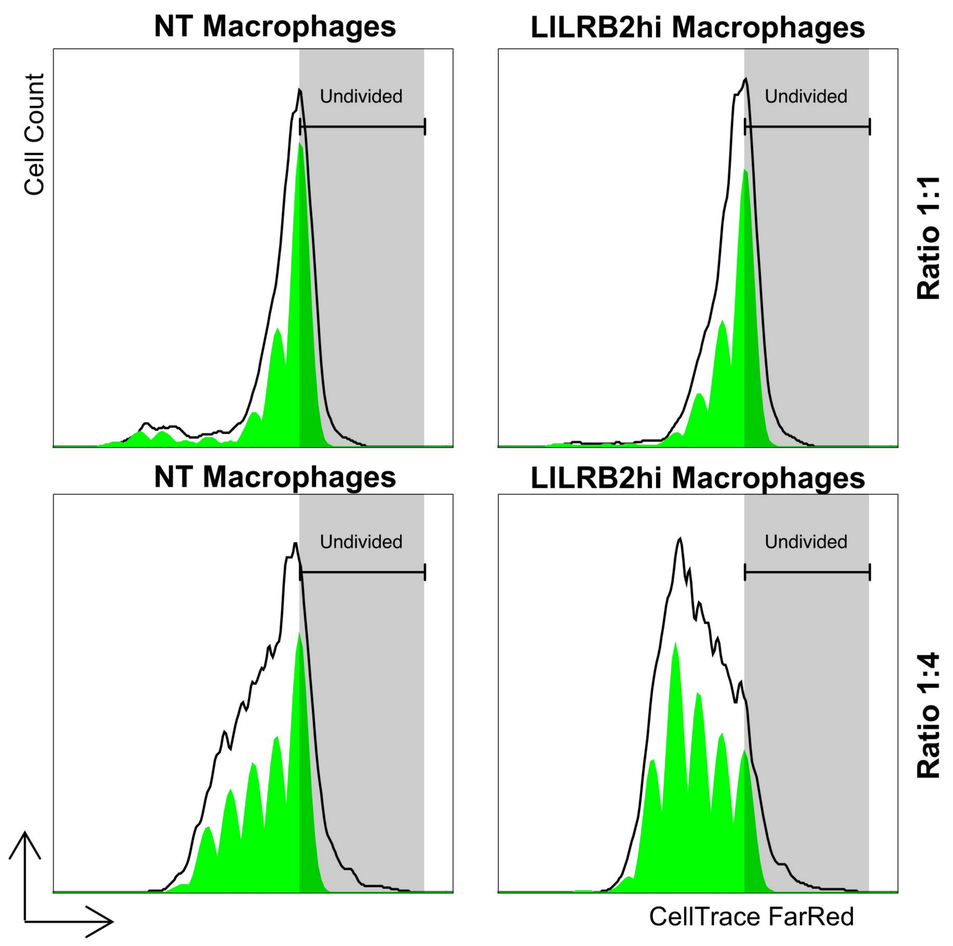

Fig.7

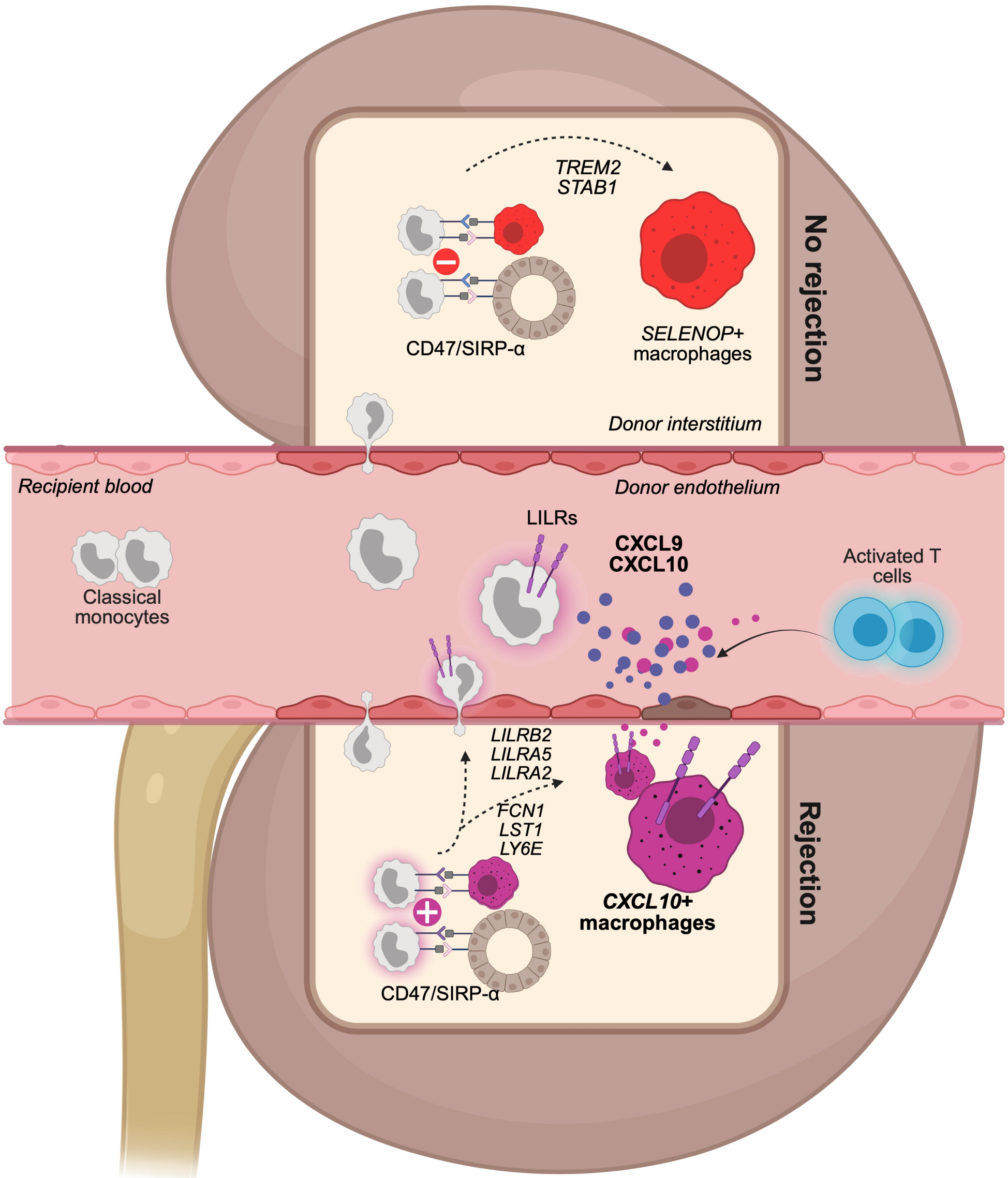
TREM2
STAB1
CD47/SIRP-α
SELENOP+
macrophages
No rejection
Donor interstitium
Recipient blood
Donor endothelium
LILRs
CXCL9
CXCL10
Activated T
cells
Classical
monocytes
LILRB2
LILRA5
LILRA2
FCN1
LST1
LY6E
CXCL10+
macrophages
Rejection
CD47/SIRP-α